

Critical spin fluctuations across the superconducting dome in $\text{La}_{2-x}\text{Sr}_x\text{CuO}_4$

Jacopo Radaelli,¹ Aavishkar A. Patel,^{2,3} Mengze Zhu,¹ Oliver J. Lipscombe,¹
J. Ross Stewart,⁴ Subir Sachdev,⁵ and Stephen M. Hayden¹

¹*H.H. Wills Physics Laboratory, University of Bristol,
Tyndall Avenue, Bristol BS8 1TL, United Kingdom*

²*International Centre for Theoretical Sciences, Tata Institute of Fundamental Research, Bengaluru 560089, India*

³*Center for Computational Quantum Physics, Flatiron Institute, 162 5th Avenue, New York, NY 10010, USA*

⁴*ISIS Pulsed Neutron and Muon Source, Rutherford Appleton Laboratory, Didcot OX11 0QX, United Kingdom*

⁵*Department of Physics, Harvard University, Cambridge, MA 02138, USA*

Overdoped cuprate superconductors are strange metals above their superconducting transition temperature. In such materials, the electrical resistivity has a strong linear dependence on temperature (T) and electrical current is not carried by electron quasiparticles as in conventional metals. Here we demonstrate that the strange metal behaviour co-exists with strongly temperature-dependent critical spin fluctuations showing dynamical scaling across the cuprate phase diagram. Our neutron scattering observations and the strange metal behaviour are consistent with a spin density wave quantum phase transition in a metal with spatial disorder in the tuning parameter. Numerical computations using a theory of spin density waves in a disordered metal yield an extended ‘Griffiths phase’ with scaling properties in agreement with experimental observations. Thus we establish that low-energy spin excitations and spatial disorder are central to the strange metal behaviour.

Understanding high-temperature superconductivity in layered cuprates has posed significant challenges to the theory of condensed matter. In particular, the unusual metallic state of cuprates above their critical temperature, T_c , remains poorly understood. This state is crucial, as superconductivity emerges from it. The underdoped region of the cuprate phase diagram is characterized by the presence of various competing orders such as antiferromagnetism (AF), charge density wave (CDW) order, and the pseudogap state [1]. In contrast, the overdoped region is free from competing phases, but its normal state ($T > T_c$) shows “strange metal” (SM) behaviour [2] where the resistivity, ρ , is proportional to temperature, T , with a large proportionality constant.

The resistivity of a metal is usually interpreted using the Drude model in which $\rho \propto \tau_{\text{tr}}^{-1}$, where τ_{tr}^{-1} is the relaxation rate of the electrons transporting current. SM behaviour occurs in many classes of material [3] where it has been found that τ_{tr}^{-1} is approximately equal to $k_B T / \hbar$, the Planckian dissipative rate [4]. This is in stark contrast to the $\rho \propto T^2$ and $\tau_{\text{tr}}^{-1} \propto T^2$ expected to describe metals in Fermi liquid theory at low temperature. The SM [3] in resistivity can be accompanied by an anomalous specific heat contribution $C \propto T \ln(1/T)$ in contrast to the liquid Fermi form $C \propto T$.

The existence of SM behaviour over a wide T range in cuprates is challenging for theory to explain [5]. The picture in simple metals is based on the current-carrying fermion quasiparticles near the Fermi surface scattering off bosons (e.g. phonons). Phonons can only give a linear behaviour at high temperatures $T \gtrsim \theta_{\text{Debye}}$ where all phonon modes are excited. Electron-electron scattering yields $\rho \propto T^2$ because only electrons within $k_B T$ of the Fermi surface scatter. In addition, the Planckian dissi-

pation mentioned above implies that quasiparticles lose coherence in the shortest time allowed by quantum mechanics and that the quasiparticle concept breaks down.

Here we show that nearly-critical low-energy collective spin fluctuations are central to the strange metal behaviour in the cuprates and exist across the superconducting dome. We investigate the overdoped region of a cuprate superconductor where the SM behaviour is clearest [6]. The material we have chosen is $\text{La}_{2-x}\text{Sr}_x\text{CuO}_4$ (LSCO). This system can be hole-doped over a wide range through the overdoped region of the phase diagram (Fig. 1A) and has a relatively low T_c so that the SM normal state is present over approximately two orders of magnitude in temperature.

RESULTS

Spin fluctuations in cuprates

Spin fluctuations have been widely studied in LSCO and other cuprate superconductors by techniques such as inelastic neutron scattering, resonant inelastic x-ray scattering and nuclear magnetic resonance [12]. The parent compounds such as La_2CuO_4 are antiferromagnetic with strong super-exchange coupling, J , and spin wave excitations [13] up to ~ 320 meV. Upon doping these spin wave-excitations become heavily damped, with residual antiferromagnetic or spinon excitations remaining at higher energies $\gtrsim 100$ meV [9, 10] as illustrated schematically in Fig. 1B. In addition to the band of higher energy excitations, doped cuprates show low-energy excitations which are highly structured in reciprocal space [14] with the strongest excitations at $\mathbf{Q}_\delta = (1/2, 1/2 \pm \delta)$ and $(1/2 \pm \delta, 1/2)$. For underdoped compositions, with

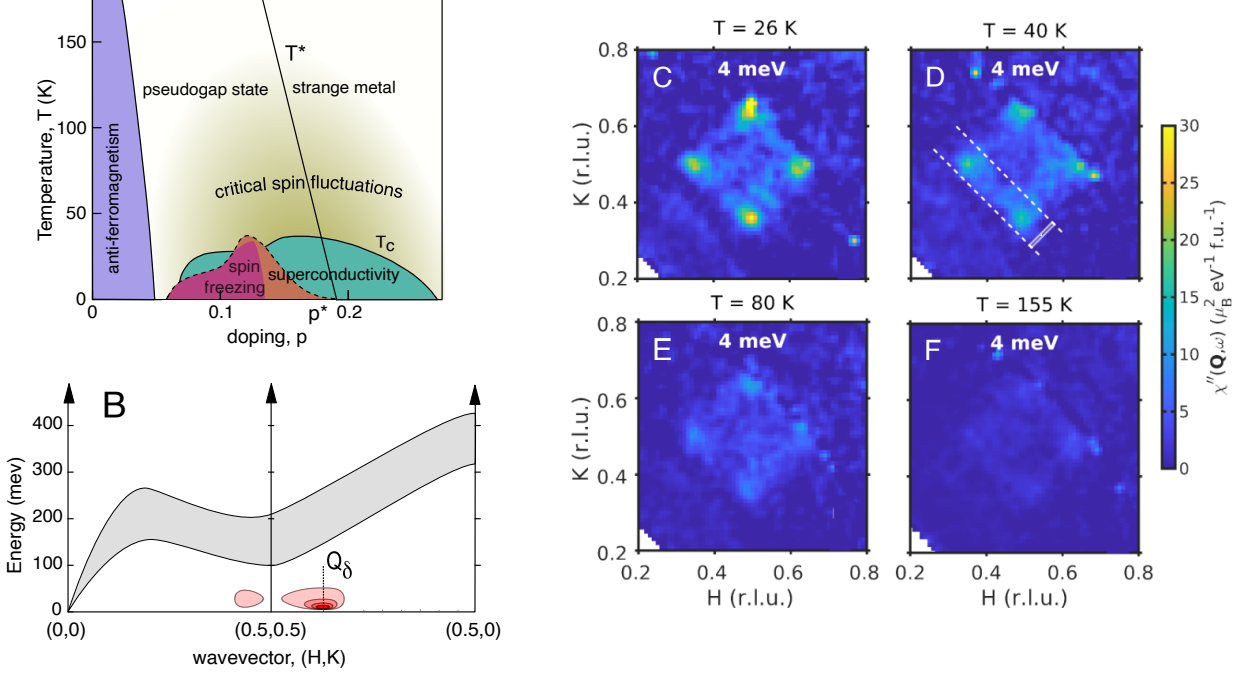


FIG. 1. **Spin fluctuations in $\text{La}_{2-x}\text{Sr}_x\text{CuO}_4$ ($x=0.22$).** (A) Schematic phase diagram of LSCO showing the possible extent of the critical spin fluctuations observed here. The dashed line shows the extent of spin freezing for $B = 80$ T [7] where superconductivity is fully suppressed and the magenta region for $B = 0$ from Ref. [8]. (B) Schematic of spin excitations in LSCO ($x = 0.22$) based on (Refs. [9, 10]) as represented by contours of the imaginary part of the susceptibility $\chi''(\mathbf{Q}, \omega)$. Reciprocal space is labelled as $\mathbf{Q} = H\mathbf{a}^* + K\mathbf{b}^* + L\mathbf{c}^* \equiv (H, K)$. The gray region shows the broad high-energy spin excitations [9, 10]. Pink regions are the low-energy excitations studied here. (C-F) Slices of $\chi''(\mathbf{Q}, \omega)$ for $\hbar\omega = 4$ meV, $L \in [-1, 1]$ and various temperatures (see Methods for details). The white rectangle in (D) shows the region of integration used to produce the points in 1-D cuts such as those in Fig. 2A, with integration along (1,1). Dashed lines represent the path of the 1-D cuts.

doping $x = p \sim 1/8$, these incommensurate spin fluctuations freeze for $T \lesssim T_c$ [7, 15, 16]. At higher temperatures in the normal state they are strongly temperature dependent showing the hallmarks of proximity to quantum criticality such as ω/T -scaling [11, 17, 18]. For overdoped LSCO, low-energy spin fluctuations were observed to grow monotonically down to $T \approx T_c$ [19]. For LSCO ($x = 0.22$) and $T \approx T_c = 26$ K, it was recently found [20] that these excitations are described by a heavily over-damped harmonic oscillator response and have a characteristic energy scale $\hbar\Gamma_\delta \approx 5$ meV $\approx 3k_B T$.

We used inelastic neutron scattering to map out the \mathbf{Q} - ω dependence of the low-energy spin fluctuations in single crystals of LSCO ($x=0.22$) in the normal state for temperatures $T_c \leq T \leq 300$ K. Measurements were carried out using the LET spectrometer of the ISIS Pulsed Neutron and Muon Source (See Methods). Fig. 1C-F show constant energy maps of the dynamic susceptibility $\chi''(\mathbf{Q}, \omega)$ at $\hbar\omega = 4$ meV. For $T = 26$ K, the four-peaks around $\mathbf{Q} = (1/2, 1/2)$ can be clearly seen in Fig. 1C. Cuts through the peaks along the $\mathbf{Q} = (1/2 - \delta/2 + \xi, 1/2 - \delta/2 + \xi)$ line (along the cen-

tre of dashed lines in Fig. 1D) are shown in Fig. 2A. As the temperature increases, the peaks can be seen to weaken and broaden in \mathbf{Q} . The measured intensity $S(\mathbf{Q}, \omega)$ can be converted to the magnetic response function $\chi''(\mathbf{Q}, \omega)$ using the fluctuation dissipation theorem $S(\mathbf{Q}, \omega) = (1/\pi)\chi''(\mathbf{Q}, \omega)[1 - \exp(-\hbar\omega/k_B T)]^{-1}$ (See Methods), this is shown in Fig. 2B and Fig. 3A. Our data (see Fig. 3A) show that the dynamic spin susceptibility near \mathbf{Q}_δ is strongly temperature dependent for this overdoped cuprate. The behaviour is reminiscent of the approach to a quantum critical point as $T \rightarrow 0$.

Modelling the low-energy spin fluctuations

At a quantum critical point, the dynamical susceptibility is expected to have the following scaling form [21]

$$\chi(q, \omega) \propto T^{-\alpha} \Phi\left(\xi q, \frac{\hbar\omega}{k_B T}\right), \quad (1)$$

where $\xi \propto T^{-1/2}$ is a correlation length, z is the dynamic critical exponent, $\mathbf{q} = \mathbf{Q} - \mathbf{Q}_\delta$ is the wavevector relative

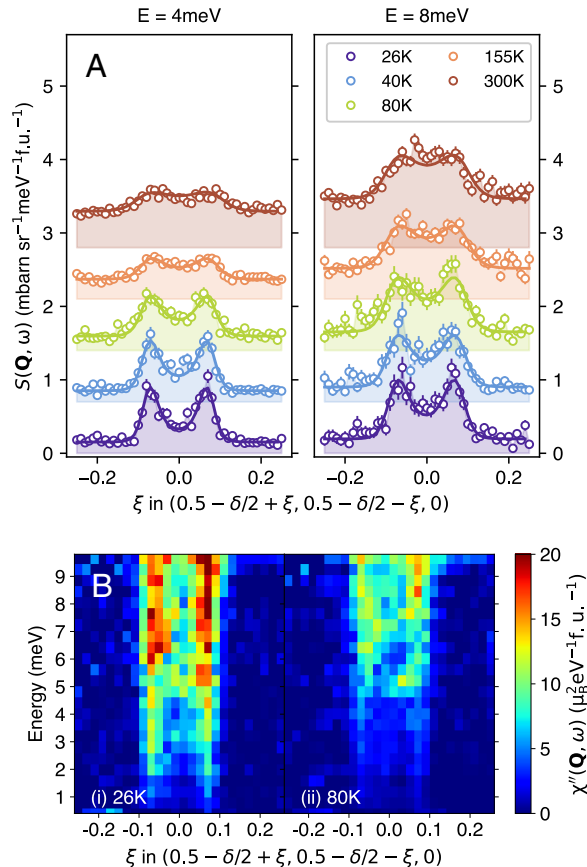


FIG. 2. **The temperature dependence of the low-energy spin fluctuations in $\text{La}_{2-x}\text{Sr}_x\text{CuO}_4$ ($x=0.22$).** (A) The scattering intensity versus wavevector \mathbf{Q} for different temperatures (bottom to top: 26, 40, 80, 155, 300 K) for energy transfers $\hbar\omega = 4, 8$ meV. The cuts are through the incommensurate \mathbf{Q}_δ positions as shown by the dashed lines in Fig. 1D. (B) $E - \mathbf{Q}$ map of the magnetic response function $\chi''(\mathbf{Q}, \omega)$ for $T = 26, 80$ K showing its evolution with temperature. The trajectory of \mathbf{Q} is the same as that in (A).

to the ordering wavevector, $q = |\mathbf{q}|$ and Φ is a universal complex function of both arguments. For $q = 0$, the imaginary part of the dynamical susceptibility (measured here) has the following scaling form (See Supplementary Methods):

$$\chi''(q=0, \omega) = T^{-\alpha} \phi_1\left(\frac{\hbar\omega}{k_B T}\right), \quad (2)$$

where $\alpha = \gamma/\nu z$, $\phi_1(x) = \Im[\Phi(0, x)]$ is a scaling function and γ and ν are the susceptibility and correlation function temperature exponents respectively. This is an example of ω/T -scaling.

In Fig. 3B we show that our data can be collapsed onto a single trend with a suitable choice of α . An analogous collapse is observed in heavy fermion systems [22, 23].

In our case, $\phi_1(x)$ can be approximated by a simple Lorentzian $\phi_1(x) \propto ax/(a^2 + x^2)$ with $a = 2.9 \pm 0.3$ and $\alpha = 0.32 \pm 0.10$. This small value of α excludes the familiar paramagnon theory which has $\alpha = 1$ [24, 25] and does not show an extended regime of criticality. Our data are consistent with the measured susceptibility having a low-frequency component that varies as

$$\chi''(\mathbf{Q}_\delta, \omega) = \frac{\chi'(\mathbf{Q}_\delta)\Gamma_\delta \omega}{\Gamma_\delta^2 + \omega^2}, \quad (3)$$

where the real part of the susceptibility $\chi'(\mathbf{Q}_\delta) \propto T^{-\alpha}$ and the spin relaxation rate varies as

$$\hbar\Gamma_\delta = ak_B T, \quad (4)$$

as shown in Fig. 3A(inset). Thus our data are consistent with Γ_δ tracking the Planckian relaxation rate $\tau_{\text{tr}}^{-1} \propto T$ as observed in transport measurements suggesting that they are related.

More information about the criticality of the spin fluctuations can be gained from the \mathbf{Q} -dependence of $\chi''(\mathbf{Q}, \omega)$. We fitted our data using a form previously used [11, 20] to describe the low-energy response of the cuprates:

$$\chi''(\mathbf{Q}, \omega) = \chi''(\mathbf{Q}_\delta, \omega) \frac{1}{[1 + \kappa^{-2}(\omega)R(\mathbf{Q})]^2}, \quad (5)$$

where $R(\mathbf{Q})$ is a function with zeros at the \mathbf{Q}_δ positions and $R(\mathbf{Q}) = |\mathbf{q}|^2$ near $\mathbf{Q} = \mathbf{Q}_\delta$ [see Supplementary Equation (11)]. Eqn. 5 has peaks at the four \mathbf{Q}_δ positions and $\kappa(\omega)$ is a measure of the peak width. Example fits to Eqn. 5 are shown in Fig. 2 and the resulting values of $\kappa(\omega)$ are shown in Fig. 3D,E,F. Eqns. 1 and 5 taken together (See Supplementary Methods) imply an additional κ -scaling

$$\kappa(\omega) = T^{\frac{1}{z}} \phi_2\left(\frac{\hbar\omega}{k_B T}\right) \quad (6)$$

and $\kappa(0) \propto T^{\frac{1}{z}}$.

In Fig. 3D we see that $\kappa(\omega)$ increases with ω and T . We posit that the effects of ω and T add as

$$\kappa^2(\omega) \propto (\hbar\omega)^{2/z} + r(k_B T)^{2/z}, \quad (7)$$

where r is the ratio of the temperature and energy contributions which we set equal to one. This form satisfies Eqn. 6. We find that Eqn. 7 can be used to collapse the experimentally determined $\kappa(\omega, T)$ onto a single solid line as shown in Fig. 3E,F with $z = 1.83 \pm 0.35$. In the Supplementary Methods we show that our data are also consistent with the system being tuned slightly away from quantum criticality (dashed line in Fig. 3F) within the uncertainty of the experiment.

Here we only study the normal state, however, we can extrapolate the data to lower temperatures. Fig. 3 suggests that the spin fluctuations would continue to evolve

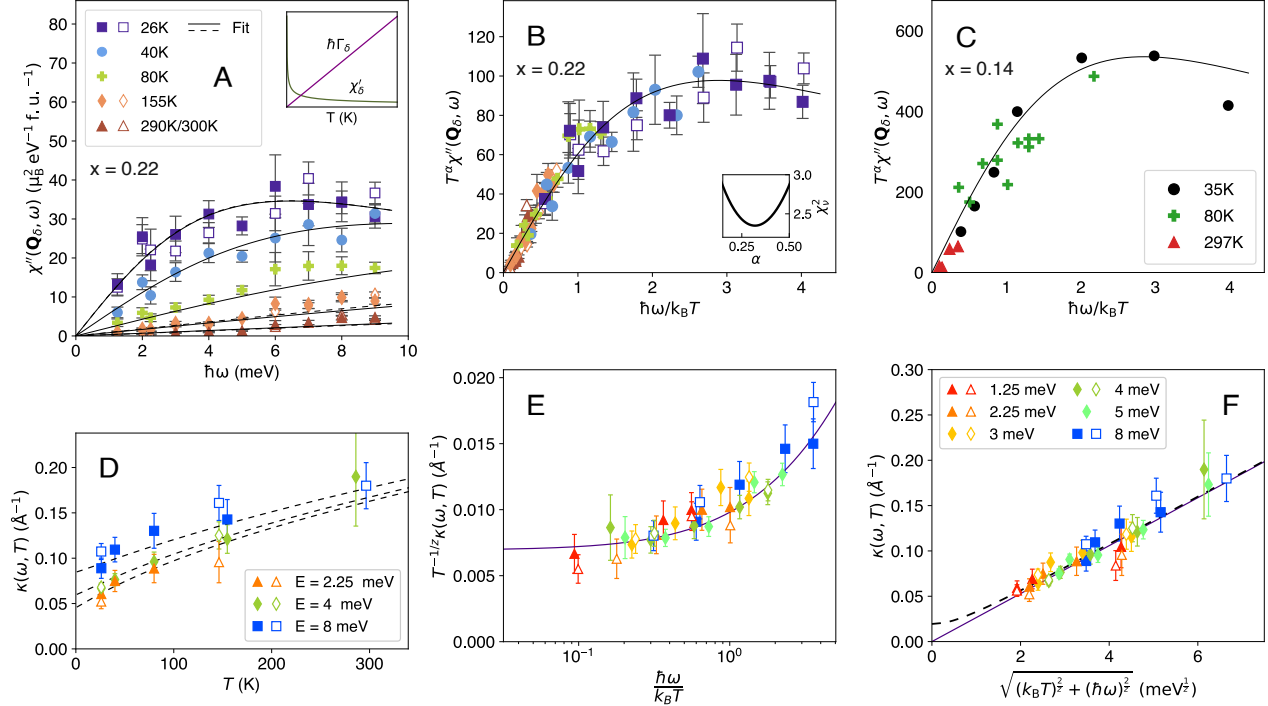


FIG. 3. **Scaling behaviour of the dynamic magnetic susceptibility and correlation length in $\text{La}_{2-x}\text{Sr}_x\text{CuO}_4$** (A) Temperature dependence of $\chi''(\mathbf{Q}_\delta, \omega)$ at ordering wavevector \mathbf{Q}_δ . Lines are fits to Eqn. 3. Open and closed symbols are two separate experiments. Inset shows the T -dependence of the spin relaxation rate Γ_δ and real part of the susceptibility $\chi'(\mathbf{Q}_\delta)$ obtained when data are modelled with Eqns. 3-4. (B) ω/T -scaling plot of the $x = 0.22$ data in (A) using Eqn. 2 and the procedure described in Methods. The inset shows how the quality of the collapse varies with exponent α . (C) Scaling plot for underdoped LSCO $x = 0.14$ data from Ref. [11]. This data shows a similar collapse to the $x = 0.22$ data in (B). (D) The width in \mathbf{Q} of $\chi''(\mathbf{Q}, \omega)$ is denoted by the inverse dynamic correlation length $\kappa(\omega)$. Here we plot $\kappa(\omega, T)$ versus temperature for $\hbar\omega = 1.25, 2.25, 4, 8$ meV. (E) Data in (D) can be collapsed onto a single trend line with suitable choice of z and ω/T -scaling. (F) Data in (D) can be scaled onto a single line using (7) allowing the dynamic critical exponent z to be determined. Dashed line is Supplementary Equation 15.

as $T \rightarrow 0$ in the absence of superconductivity. This is supported by measurements made where superconductivity is suppressed by a magnetic field. Previous neutron scattering measurements [20] show that Γ_δ continues to decrease below T_c when a 9 Tesla field is applied. High field ($B \gtrsim B_{c2}$) heat capacity measurements show a $\sim T \log(1/T)$ contribution [26] and resistivity measurements in a high field [6] show a $\rho \propto T$ behaviour for T going to zero.

Thus we have found that the low-energy spin fluctuations of the overdoped superconductor LSCO ($x = 0.22$) show the hallmarks of quantum criticality. Specifically, we observe that both $\chi''(q = 0, \omega)$ and $\kappa(\omega)$ show ω/T -scaling. The dynamical critical exponent is $z = 1.83 \pm 0.35$. Our value of z for LSCO ($x = 0.22$) is consistent with the $z = 2$ value expected [24, 25] for a 2D antiferromagnetic metal at a QCP with coupling between electrons and spin fluctuations. It is important to view this result in the context of the whole cuprate

phase diagram. Previous T -dependent measurements in the normal state of underdoped LSCO ($x = 0.14$) [11] show a related ω/T -scaling when replotted and analysed in same way as the present data. The LSCO ($x = 0.14$) data has a similar value of $\alpha \approx 0.32$ and a smaller dynamical critical exponent, $z \approx 1$, suggesting that z increases with doping. Combining the results of the two studies we conclude that the normal state hosts low-energy critical fluctuations across the phase diagram as illustrated in Fig. 1A.

DISCUSSION

Understanding the strange metal behavior seen in LSCO and other cuprates is one of the major challenges in condensed matter physics. It occurs across a diverse set of materials that include transition metal oxides, heavy fermions [27, 28], iron-based superconductors

and twisted bilayer graphene [2, 3]. Planckian dissipation provides a universal phenomenology representing a quantum limit on the current-carrying degrees of freedom of a metal [4]. However, it does not indicate a microscopic mechanism. The behaviour in the resistivity has often been associated with an underlying magnetic quantum critical point (QCP) at $T = 0$. In a typical scenario the system is tuned to the QCP and strange metal behaviour is observed over a relatively small range of parameter space. This is observed in some systems such as $\text{Sr}_3\text{Ru}_2\text{O}_7$ [29, 30]. However, there are many examples including not only cuprates but twisted-layer graphene and twisted transition-metal dichalcogenides where it persists over an extended region. Thus alternative explanations must be explored.

The phase diagram of LSCO consists of a region of glassy incommensurate spin-freezing [7, 15, 16, 31] near $p \approx 1/8$ (also seen in other cuprates [32]). The spin freezing competes with superconductivity and when the superconductivity is suppressed by a large magnetic field $B \sim B_{c2}$ the region of spin freezing is expanded to $p \approx 0.19 \approx p^*$ (see Fig. 1A). This region reflects how the system might behave in zero field if the superconducting state did not form. The presence of an extended region of criticality as a function of doping at higher temperatures together with a disappearing frozen state at low temperatures is reminiscent of a ‘quantum Griffiths phase’ [33–35] as illustrated in Fig. 4A. A Griffiths phase [33, 35] occurs near a continuous phase transition in systems with quenched disorder. The inclusion of disorder is logical in the $\text{La}_{2-x}\text{Sr}_x\text{CuO}_4$ system because of the perturbation caused by Sr doping in the plane neighbouring the CuO_2 plane. The Griffiths phase [33, 35] corresponds to a smearing of singular behaviour as a function of a control parameter. It can naturally lead to an extended region of slow dynamics as observed in LSCO.

Here we consider the scenario where the disorder in LSCO leads to Griffiths behaviour and can be modelled by a Hertz-Millis theory [25, 39] for the onset of magnetic order in metals in the presence of spatial disorder in the tuning parameter. The dominant source of disorder in such a theory is of the ‘random mass’ type, by which local regions are tuned away from the quantum critical point of the clean system. As reviewed in the Supplementary Methods, such a theory was studied by a numerically exact treatment of disorder, but with a mean-field treatment of self-interactions of the magnetic order fluctuations [36]. This treatment is inspired and justified by the mapping of such models onto two-dimensional Yukawa-Sachdev-Ye-Kitaev models (2D-YSYK), and the latter have been treated by SYK methods and exact quantum Monte Carlo simulations, with similar results [5, 37, 38, 40].

It has been shown that the inclusion of disorder (in the 2D-YSYK and related models) can explain the existence of the SM-behaviour down to the lowest temperatures

and over an extended range of doping [36, 37]. Applying this general picture to the cuprates, it is postulated that disorder delays the onset of long range spin order giving rise to a ‘quantum Griffiths phase’ [34, 36, 37, 41, 42] (similar to that in the two-dimensional Ising model in a transverse field [43]) as a transition tuning parameter λ is reduced. SM linear-in- T resistivity is observed over an extended range of λ that comprises part of the Griffiths phase instead of a QCP. The tuning parameter λ is controlled by the doping x .

In addition to the strange metal behaviour in the resistivity observed in LSCO and other cuprates, another important property is the optical conductivity $\sigma(\omega)$. An extended Drude analysis shows that the optical scattering rate $\tau_{\text{op}}^{-1}(\omega)$ is strongly frequency dependent [44, 45] indicating the current-carrying electrons are scattered inelastically. This is incompatible with elastic scattering from impurities or defects. Phonon scattering cannot produce the T -linear resistivity at low temperature below the Debye temperature scales. This leads to the conclusion that disorder in strange metals must scatter electrons inelastically, which is predicted by the 2D-YSYK theory [5, 38]. The optical scattering rate $\tau_{\text{op}}^{-1}(\omega)$ provides a further insight into the nature of strange metals as it is found to show ω/T -scaling (along with the magnetic response reported here) over a wide range of ω/T [45].

In Fig. 4(A-D) we show numerical calculations of the critical spin susceptibility $\chi''(\mathbf{Q}_\delta, \omega)$ from the Hertz-Millis model with spatial disorder in the tuning parameter. The form in Eqn. 5 is an excellent fit to this theory (See Supplementary Methods) and allows the determination of $\kappa(\omega, T)$, which is also shown. The results have been scaled in the same way as Fig. 3B,E and we find excellent real frequency scaling at the quantum critical value of the tuning parameter $\lambda = \lambda_c = -0.4586$ with $\alpha = 0.84$ and $z = 2.13$. Corresponding scaling plots within the quantum Griffiths phase, $\lambda_G \geq \lambda > \lambda_c$, appear in the Supplementary Figures: the ω/T -scaling is still present, but it is better at smaller values of ω/T , and for the local spin susceptibility. The better scaling of the local susceptibility is as expected from the localized nature of the spin fluctuations in the Griffiths region. The value of the exponent α decreases significantly with increasing λ , down to $\alpha \approx 0.5$ at the beginning of the quantum Griffiths phase where $\lambda = \lambda_G = -0.43$. A separate, and in principle, exact determination of α is obtained from the imaginary frequency (Ω_m) susceptibility of the quantum Monte Carlo results of Ref. [37] (Fig. 4E). This also obeys Ω_m/T scaling and yields $\alpha \approx 0.2$ in the Griffiths region, compatible with our observations at $x = 0.22$. We note that ω/T -scaling fails in our theory at very low T (See Supplementary Methods), as it does in the Ising model in a transverse field [43], presumably due to the dominance of rare regions: future observations at even lower T are therefore of interest.

We now turn to the resistivity $\rho(T)$ induced by the dis-

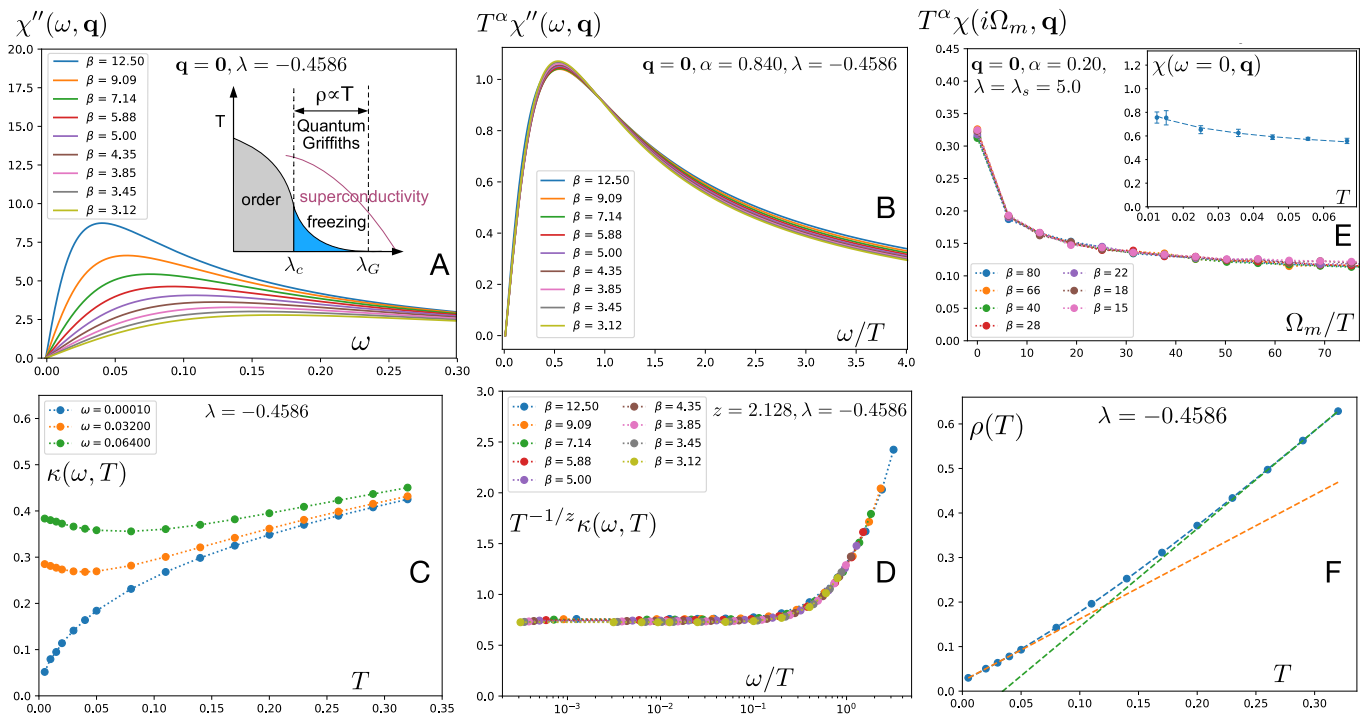


FIG. 4. **Numerical theoretical results for low energy spin fluctuations.** (A-D) (A-B) Dynamic spin susceptibility and its scaling plot, with best-fit exponent $\alpha = 0.84$. The inset in panel A provides a schematic phase diagram of the model. (C-D) Inverse correlation length κ and its scaling plot, with best-fit critical exponent $z = 2.128$. κ is in units of the inverse lattice spacing. We estimate ≈ 33 meV as the unit of energy/frequency/temperature in the numerics and $\beta = 1/T$. Theory plots should be compared with the experimental plots in Fig. 3A, B, C, D, E. Plots based on Hertz-Millis model with spatial disorder are obtained from the results of Ref. [36] (with a mean-field treatment of interactions, but exact treatment of disorder), at the critical value of $\lambda = \lambda_c = -0.4586$, after exact analytic continuation to real frequencies (See Supplementary Methods); results for $\lambda > \lambda_c$ are in the Supplementary Methods. (E) Computations of imaginary frequency (Ω_m) susceptibility by (in principle, exact) quantum Monte Carlo (QMC) results for the YSYK model in Ref. [37], at the end of the strange metal quantum Griffiths phase that is present for $\lambda_s = 5.0 \leq \lambda \leq \lambda_G = 5.5$. In the QMC results, the transition into an ordered phase at the critical point λ_c is replaced with a transition into a phase with glassy short-range order at λ_s . The dashed line in the inset is a fit to $\sim T^{-\alpha}$. Both plots yield $\alpha = 0.20$. The energy unit for the QMC computations is the fermion hopping $t \approx 0.3$ eV. (F) **Resistivity from spin fluctuations.** The resistivity is computed from the spin susceptibility, as described in Ref. [36]. Note the distinct slopes of linear-in- T resistivity at low and high T . Using the energy unit of ≈ 33 meV and the parameters of Ref. [38], with the fermion hopping $t \approx 0.3$ eV and the variance of the random Yukawa coupling $g'^2 = 4t$, the largest resistivity shown in the plot is $\approx 0.15 h/e^2$.

ordered spin fluctuations. In 2D-YSYK theory, $\rho(T)$ is determined by the imaginary part of the fermion self energy from spin fluctuations [36]. By computing this self energy, the Hertz-Millis model with spatial disorder in the tuning parameter is able to produce a linear resistivity and Planckian behaviour in the transport and optical scattering rates [36] yielding a consistent picture of the strange metal, as shown in Fig. 4F, with similar results at other values of λ in the quantum Griffiths phase shown in the Supplementary Methods. There is linear-in- T behaviour, but with different slopes at lower and higher T : we can identify these with the ‘foot’ and ‘fan’ regimes, associated with Griffiths and marginal Fermi liquid behaviours respectively [6, 45, 46]. The low T upturn in Fig. 4C in κ for $\omega > T$ is possibly also related to the crossover between these ‘foot’ and ‘fan’ regimes.

In summary, we have observed critical spin fluctua-

tions with ω/T -scaling in an overdoped cuprate superconductor. When combined with earlier measurements [11] this shows that there is an extended region of critical spin-fluctuations in $\text{La}_{2-x}\text{Sr}_x\text{CuO}_4$. We have compared our observations with numerical studies of a Hertz-Millis model for the onset of spin density wave order in a disordered metal and found good agreement. Both experiment and theory/numerics find an extended Griffiths phase of both ω/T magnetic susceptibility scaling [in $\chi''(\mathbf{Q}_\delta, \omega)$ and $\kappa(\omega)$] and T -linear resistivity. Such scaling is present even though there is no criticality in the usual sense of a diverging correlation length (See Supplementary Methods), and is accompanied by scaling deviations consistent with Griffiths physics, where scaling is violated by a logarithmic dependence on energy scales or doping [34, 37, 42]. The correlation length diverges at the lower doping boundary of the Griffiths region, and

the large correlation length allows definition of a finite dynamic exponent z which is doping (tuning parameter) dependent.

The spin excitations show $z \approx 2$, and have a contribution consistent with a spin relaxation rate $\hbar\Gamma_\delta \approx 3k_B T$. The observations may be related to singular charge density fluctuations observed in EELS [47]. The strongly T -dependent spin fluctuations coexist with transport properties described by Planckian dissipation, showing the spin degrees of freedom in the presence of spatial disorder are at the heart of strange metal behaviour. It would be interesting to study the role of such critical spin fluctuations in high temperature d -wave superconductivity [48]: it is plausible that the localization of the spin fluctuations plays a role in the near co-incident disappearance of strange metal behaviour and superconductivity with increasing doping in the cuprates [49].

METHODS

Single-crystal sample growth and characterization

Single crystals of $\text{La}_{2-x}\text{Sr}_x\text{CuO}_x$ ($x = 0.22$) were grown by the travelling-solvent floating-zone method. The crystals were annealed in 1 bar of flowing oxygen at 800°C for six weeks. The Sr concentration was determined by scanning electron microscopy with electron probe micro-analyzer (SEM-EPMA) and inductively coupled plasma atomic emission spectroscopy (ICP-AES) to be $x = 0.215 \pm 0.005$. SQUID magnetometry measurements show that $T_{c,\text{onset}} = 26\text{K}$. The sample consists of 29.8g of LSCO crystal, mounted and co-aligned using the ALF single crystal diffractometer.

Inelastic neutron scattering

Inelastic neutron scattering measurements were performed at the LET direct time-of-flight spectrometer at ISIS. LET is a multiplexing instrument which allows for simultaneous collection of data at multiple neutron incident energies. Three fixed incident energies $E_i = 3.76, 6.82, 16.02$ meV were used for the whole data collection.

To this end, the sample was mounted with its c -axis vertical and the azimuthal angle swept over a range of $\sim 108^\circ$ about the region of interest. Measurements were taken at one degree intervals to ensure adequate coverage over the entire region around the $(1/2, 1/2)$ wavevector.

Two experiments were performed. In ‘Experiment 1’ we measure at 5 different temperatures including room temperature (290K) and the superconducting transition temperature (26K). In Experiment we measured at 3 of the 5 original temperatures with the sample rotated by 90° with respect to Experiment 1 and counted for a longer period at 300 K.

Data Analysis

The scattering cross-section is related to the scattering function $S(\mathbf{Q}, \omega)$ and energy- and wavevector-dependent magnetic response function $\chi''(\mathbf{Q}, \omega)$ by the fluctuation-dissipation theorem

$$\begin{aligned} \frac{k_i}{k_f} \frac{d^2\sigma}{d\Omega dE} &= S(\mathbf{Q}, \omega) \\ &= \frac{2(\gamma r_e)^2}{\pi g^2 \mu_B^2} |F(\mathbf{Q})|^2 \frac{\chi''(\mathbf{Q}, \omega)}{1 - \exp(-\hbar\omega/k_B T)} + \text{B.G.}, \end{aligned} \quad (8)$$

where $(\gamma r_e)^2 = 0.2905$ barn sr^{-1} and $F(\mathbf{Q})$ the magnetic form factor. B.G. is non-magnetic background scattering such as incoherent inelastic phonon scattering and multiple scattering. Counts measured at position sensitive detectors were normalized to a vanadium standard to correct for differences in detector efficiency and then used to reconstruct the momentum and energy-dependent scattering function $S(\mathbf{Q}, \omega)$. This process was repeated for each E_i producing three 4-D datasets at each temperature.

1-D \mathbf{Q} Cuts and fitting

In order to parameterise the excitations for a given ω and T , $S(\mathbf{Q}, \omega)$ data slices are binned into 1-D \mathbf{Q} -dependent cuts. Cuts were made primarily through the low Q peaks at $(1/2, 1/2 - \delta)$ and $(1/2 - \delta, 1/2)$, with similar results obtained from cuts through $(1/2, 1/2 + \delta)$ and $(1/2 + \delta, 1/2)$. The cuts are generated by integrating along the \mathbf{Q} -direction perpendicular to the cut (see Fig. 1D) in the $H - K$ plane. The integral along \mathbf{c}^* was $\Delta L = \pm 1$ and in energy $\Delta E = \pm 0.5$ meV. The trajectory of the cut minimises the variation of Q and hence the variation of background due to incoherent one-phonon scattering.

We carry out a resolution-corrected least-squares fits (see Fig. 2A and Supplementary Fig. 10) to each cut using the Tobyfit module in Horace [50]. The susceptibility is modelled by Eqn. 5 and Eqn. 8. There are three energy-dependent parameters: $\chi''(\mathbf{Q}_\delta, \omega)$ and $\kappa(\omega)$ which control the height and width of the peaks in \mathbf{Q} respectively, and a \mathbf{Q} -independent (constant) background. From the fits in Fig. 2A and Supplementary Fig. 10 it can be seen that the background increases with ω and T consistent with one-phonon incoherent scattering from the sample.

The incommensurability δ of the excitations also enters into the model via $R(\mathbf{Q})$. The value of δ in Eqn. 5 and Supplementary Equation (11) was fixed for each temperature. The fitted values ranged from $\delta = 0.139$ to $\delta = 0.131$ for $T = 26$ and 300 K respectively. When making T -dependent (scaling) plots we evaluated the fitted $\chi''(\mathbf{Q}_\delta, \omega)$ for the $T = 26$ K value of δ . This was determined by averaging over energy dependent best-fit values below 5meV where the peaks are sharp.

ω/T scaling collapse

For a given α value, we calculated a set of scaled peak susceptibilities $y_i(\omega/T) = T^\alpha \chi_i''(\mathbf{Q}_\delta, \omega/T)$. These were placed in evenly spaced bins in $x = \hbar\omega/k_B T$ between $x = 0$ and $x = 4$. The y_i -values were compared against a function $E(x_i)$, calculated using the bin averages and bin centres for that α , to give a reduced chi-squared,

$$\chi_v^2 = \frac{1}{N} \sum_{i=1,N} \frac{[y_i - E(x_i)]^2}{\sigma_i^2},$$

where $E(x)$ was a piecewise function with linear segments connecting the $(\tilde{x}_j, \tilde{y}_j)$ points where \tilde{x}_j and \tilde{y}_j are the bin centres and bin averages respectively. We then determine the α that minimises χ_v^2 .

2-D \mathbf{Q} and \mathbf{Q} -E Slices

To produce the 2-D \mathbf{Q} slices for display in Fig. 1C-F, data is integrated over $L = \pm 1$ and $\Delta\hbar\omega = \pm 0.5$ meV. $S(\mathbf{Q}, \omega)$ is converted to $\chi''(\mathbf{Q}, \omega)$ using Eqn. 8 following subtraction of a \mathbf{Q} -independent background determined from the 1-D fitting described above. A similar procedure is used for the $\mathbf{Q} - \omega$ plot in Fig. 2C except that $\Delta\hbar\omega = \pm 0.25$ meV and a different background (determined from the 1-D \mathbf{Q} -cuts) was used for each energy.

Phonon Scattering

Inelastic neutron scattering also detects phonon scattering due to the interaction of the neutron with the nucleus. One-phonon coherent scattering yields well defined peaks in (\mathbf{Q}, ω) and one-phonon incoherent yields smooth variation in (\mathbf{Q}, ω) . The intensity of both types of one-phonon scattering are proportional to Q^2 and the Bose factor $[1 - \exp(-\hbar\omega/k_B T)]^{-1}$.

In order to minimize the effect of phonons, we (i) performed the experiment in the first Brillouin zone, (ii) measured for $\hbar\omega \leq 10$ meV where there are relatively few phonons. The scattering we observe is two dimensional. We used a small integral in L to minimize the phonon scattering. Supplementary Fig. 12 shows the magnetic scattering measured near $L = 0$ compared with the phonons measured near $L = 4$ for a 1-D cut with the same (H, K) values. It can be seen that the phonons and magnetic scattering have very different structures in (\mathbf{Q}, ω) . The magnetic scattering presents as columns of scattering and the phonons as a dispersive mode. The model we use to fit data for a particular ω [Eqn. 5, Eqn. 8 and Supplementary Equation (11)] has a different shape in \mathbf{Q} to the phonon scattering. It therefore picks out the magnetic scattering as shown Fig. 2A and Supplementary Fig. 10B. However, there are some deviations which

may be due to phonon scattering e.g. near $\xi = 0$ for $T = 300$ K and $\hbar\omega = 7$ meV.

DATA AVAILABILITY

Source data for experimental figures are provided with this paper. Raw data are at <https://doi.org/10.5286/ISIS.E.RB2220248-1> and <https://doi.org/10.5286/ISIS.E.RB2410260-1>

ACKNOWLEDGEMENTS

S.M.H is grateful to Jörg Schmalian for sharing insights about scaling theory. A.A.P. and S.S. thank Peter Lunts for related collaborations. Neutron beamtime was provided by the ISIS neutron and muon source through proposals RB2220248 and RB2410260. Work was supported by the U.K. EPSRC through grant EP/R011141/1. The Flatiron Institute is a division of the Simons Foundation. S.S. was supported by the U.S. National Science Foundation grant No. DMR-2245246.

AUTHOR CONTRIBUTIONS

Single crystals were grown and characterised by O.J.L and S.M.H. Neutron scattering measurements were performed by J.R., M.Z., J.R.S. and S.M.H. Data analysis performed by J.R. and S.M.H. Numerical theory performed by A.A.P. and S.S. The paper was written by J.R., A.A.P., S.S. and S.M.H.

COMPETING INTERESTS

The authors have no competing interests associated with this paper.

-
- [1] B. Keimer, S. A. Kivelson, M. R. Norman, S. Uchida, and J. Zaanen, *Nature* **518**, 179 (2015).
 - [2] P. W. Phillips, N. E. Hussey, and P. Abbamonte, *Science* **377**, eabh4273 (2023).
 - [3] S. A. Hartnoll and A. P. Mackenzie, *Rev. Mod. Phys.* **94**, 041002 (2022).
 - [4] J. Zaanen, *Nature* **430**, 512 (2004).
 - [5] A. A. Patel, H. Guo, I. Esterlis, and S. Sachdev, *Science* **381**, 790 (2023).
 - [6] R. A. Cooper, Y. Wang, B. Vignolle, O. J. Lipscombe, S. M. Hayden, Y. Tanabe, T. Adachi, Y. Koike, M. Nohara, H. Takagi, C. Proust, and N. E. Hussey, *Science* **323**, 603 (2009).
 - [7] M. Frachet, I. Vinograd, R. Zhou, S. Benhabib, S. Wu, H. Mayaffre, S. Krämer, S. K. Ramakrishna, A. P.

- Reyes, J. Debray, T. Kurosawa, N. Momono, M. Oda, S. Komiya, S. Ono, M. Horio, J. Chang, C. Proust, D. LeBoeuf, and M.-H. Julien, *Nat. Phys.* **16**, 1064 (2020).
- [8] M. Kofu, S.-H. Lee, M. Fujita, H.-J. Kang, H. Eisaki, and K. Yamada, *Phys. Rev. Lett.* **102**, 047001 (2009).
- [9] O. J. Lipscombe, S. M. Hayden, B. Vignolle, D. F. McMorrow, and T. G. Perring, *Phys. Rev. Lett.* **99**, 067002 (2007).
- [10] H. C. Robarts, M. Barthélemy, K. Kummer, M. García-Fernández, J. Li, A. Nag, A. C. Walters, K. J. Zhou, and S. M. Hayden, *Phys. Rev. B* **100**, 214510 (2019).
- [11] G. Aeppli, T. Mason, S. Hayden, H. Mook, and J. Kulda, *Science* **278**, 1432 (1997).
- [12] M. Fujita, H. Hiraka, M. Matsuda, M. Matsuura, J. M. Tranquada, S. Wakimoto, G. Xu, and K. Yamada, *J. Phys. Soc. Jpn.* **81**, 011007 (2011).
- [13] N. S. Headings, S. M. Hayden, R. Coldea, and T. G. Perring, *Phys. Rev. Lett.* **105**, 247001 (2010).
- [14] S. W. Cheong, G. Aeppli, T. E. Mason, H. Mook, S. M. Hayden, P. C. Canfield, Z. Fisk, K. N. Clausen, and J. L. Martinez, *Phys. Rev. Lett.* **67**, 1791 (1991).
- [15] T. Suzuki, T. Goto, K. Chiba, T. Shinoda, T. Fukase, H. Kimura, K. Yamada, M. Ohashi, and Y. Yamaguchi, *Phys. Rev. B* **57**, R3229 (1998).
- [16] D. J. Campbell, M. Frachet, V. Oliviero, T. Kurosawa, N. Momono, M. Oda, J. Chang, D. Vignolles, C. Proust, and D. LeBoeuf, “Strange metal from spin fluctuations in a cuprate superconductor,” (2024), arXiv:2412.03720 [cond-mat.supr-con].
- [17] S. M. Hayden, G. Aeppli, H. Mook, D. Rytz, M. F. Hundley, and Z. Fisk, *Phys. Rev. Lett.* **66**, 821 (1991).
- [18] B. Keimer, R. J. Birgeneau, A. Cassanho, Y. Endoh, R. W. Erwin, M. A. Kastner, and G. Shirane, *Phys. Rev. Lett.* **67**, 1930 (1991).
- [19] S. Wakimoto, H. Zhang, K. Yamada, I. Swainson, H. Kim, and R. J. Birgeneau, *Phys. Rev. Lett.* **92**, 217004 (2004).
- [20] M. Zhu, D. J. Voneshen, S. Raymond, O. J. Lipscombe, C. C. Tam, and S. M. Hayden, *Nat. Phys.* **19**, 99 (2023).
- [21] S. Sachdev and J. Ye, *Phys. Rev. Lett.* **69**, 2411 (1992).
- [22] M. C. Aronson, R. Osborn, R. A. Robinson, J. W. Lynn, R. Chau, C. L. Seaman, and M. B. Maple, *Phys. Rev. Lett.* **75**, 725 (1995).
- [23] A. Schröder, G. Aeppli, R. Coldea, M. Adams, O. Stockert, H. Löhneysen, E. Bucher, R. Ramazashvili, and P. Coleman, *Nature* **407**, 351 (2000).
- [24] A. J. Millis, H. Monien, and D. Pines, *Phys. Rev. B* **42**, 167 (1990).
- [25] A. J. Millis, *Phys. Rev. B* **48**, 7183 (1993).
- [26] C. Girod, D. LeBoeuf, A. Demuer, G. Seyfarth, S. Imajo, K. Kindo, Y. Kohama, M. Lizaire, A. Legros, A. Gourgout, H. Takagi, T. Kurosawa, M. Oda, N. Momono, J. Chang, S. Ono, G.-q. Zheng, C. Marcenat, L. Taillefer, and T. Klein, *Phys. Rev. B* **103**, 214506 (2021).
- [27] M. C. Aronson, R. Osborn, R. A. Robinson, J. W. Lynn, R. Chau, C. L. Seaman, and M. B. Maple, *Phys. Rev. Lett.* **75**, 725 (1995).
- [28] W. J. Gannon, L. S. Wu, I. A. Zaliznyak, W. H. Xu, A. M. Tsvelik, Y. Qiu, J. A. Rodriguez-Rivera, and M. C. Aronson, *Proceedings of the National Academy of Science* **115**, 6995 (2018).
- [29] J. A. N. Bruin, H. Sakai, R. S. Perry, and A. P. Mackenzie, *Science* **339**, 804 (2013).
- [30] C. Lester, S. Ramos, R. S. Perry, T. P. Croft, M. Laver, R. I. Bewley, T. Guidi, A. Hiess, A. Wildes, E. M. Forgan, and S. M. Hayden, *Nat. Commun.* **12**, 5798 (2021).
- [31] J. Chang, C. Niedermayer, R. Gilardi, N. B. Christensen, H. M. Rønnow, D. F. McMorrow, M. Ay, J. Stahn, O. Sobolev, A. Hiess, S. Pailhes, C. Baines, N. Momono, M. Oda, M. Ido, and J. Mesot, *Phys. Rev. B* **78**, 104525 (2008).
- [32] T. Wu, H. Mayaffre, S. Krämer, M. Horvatić, C. Berthier, C. T. Lin, D. Haug, T. Loew, V. Hinkov, B. Keimer, and M.-H. Julien, *Phys. Rev. B* **88**, 014511 (2013).
- [33] R. B. Griffiths, *Phys. Rev. Lett.* **23**, 17 (1969).
- [34] S. Sachdev, *Quantum Phase Transitions* (Cambridge University Press, Cambridge, UK, 1999).
- [35] T. Vojta, in *Lectures on the Physics of Strongly Correlated Systems XVII: Seventeenth Training Course in the Physics of Strongly Correlated Systems*, American Institute of Physics Conference Series, Vol. 1550, edited by A. Avella and F. Mancini (AIP, 2013) pp. 188–247, arXiv:1301.7746 [cond-mat.dis-nn].
- [36] A. A. Patel, P. Lunts, and S. Sachdev, *Proc. Natl. Acad. Sci.* **121**, e2402052121 (2024).
- [37] A. A. Patel, P. Lunts, and M. S. Alberg, *Phys. Rev. X* **15**, 031064 (2025).
- [38] C. Li, D. Valentini, A. A. Patel, H. Guo, J. Schmalian, S. Sachdev, and I. Esterlis, *Phys. Rev. Lett.* **133**, 186502 (2024).
- [39] J. A. Hertz, *Phys. Rev. B* **14**, 1165 (1976).
- [40] I. Esterlis, H. Guo, A. A. Patel, and S. Sachdev, *Phys. Rev. B* **103**, 235129 (2021).
- [41] J. A. Hoyos, C. Kotabage, and T. Vojta, *Phys. Rev. Lett.* **99**, 230601 (2007).
- [42] T. Vojta, C. Kotabage, and J. A. Hoyos, *Phys. Rev. B* **79**, 024401 (2009).
- [43] O. Motrunich, S.-C. Mau, D. A. Huse, and D. S. Fisher, *Phys. Rev. B* **61**, 1160 (2000).
- [44] J. P. Carbotte, T. Timusk, and J. Hwang, *Rep. Prog. Phys.* **74**, 066501 (2011).
- [45] B. Michon, C. Berthod, C. W. Rischau, A. Ataei, L. Chen, S. Komiya, S. Ono, L. Taillefer, D. van der Marel, and A. Georges, *Nat. Commun.* **14**, 3033 (2023).
- [46] S. Sachdev, *Physica C* **633**, 1354707 (2025).
- [47] X. Guo, J. Chen, F. Hoveyda-Marashi, S. L. Bettler, D. Chaudhuri, C. S. Kengle, J. A. Schneeloch, R. Zhang, G. Gu, T.-C. Chiang, A. M. Tsvelik, T. Faulkner, P. W. Phillips, and P. Abbamonte, “Conformally invariant charge fluctuations in a strange metal,” (2024), arXiv:2411.11164 [cond-mat.str-el].
- [48] A. Abanov, A. V. Chubukov, and A. M. Finkel’stein, *Europhys. Lett.* **54**, 488 (2001).
- [49] N. Bashan, E. Tulipman, S. A. Kivelson, J. Schmalian, and E. Berg, “Extended strange metal regime from superconducting puddles,” (2025), arXiv:2502.08699 [cond-mat.str-el].
- [50] R. Ewings, A. Buts, M. Le, J. van Duijn, I. Bustinduy, and T. Perring, *Nucl. Instrum. Methods Phys. Res., Sect. A* **834**, 132 (2016).

Critical spin fluctuations across the superconducting dome in $\text{La}_{2-x}\text{Sr}_x\text{CuO}_4$

Jacopo Radaelli,¹ Aavishkar A. Patel,² Mengze Zhu,¹ Oliver J. Lipscombe,¹
J. Ross Stewart,³ Subir Sachdev,⁴ and Stephen M. Hayden¹

¹*H.H. Wills Physics Laboratory, University of Bristol,
Tyndall Avenue, Bristol BS8 1TL, United Kingdom*

²*Center for Computational Quantum Physics, Flatiron Institute, 162 5th Avenue, New York, NY 10010, USA*

³*ISIS Pulsed Neutron and Muon Source, Rutherford Appleton Laboratory, Didcot OX11 0QX, United Kingdom*

⁴*Department of Physics, Harvard University, Cambridge, MA 02138, USA*

SUPPLEMENTARY METHODS

Dynamic critical scaling theory

The dynamic susceptibility of systems below their upper critical dimension is expected to obey the following scaling behavior:

$$\chi(q, \omega, T, t) = b^{\gamma/\nu} \chi(bq, b^z \omega, b^z T, b^{1/\nu} t), \quad (\text{S1})$$

where b is an arbitrary scaling parameter, t is a tuning control parameter [$t = 0$ corresponds to the quantum critical point (QCP)], q is momentum relative to ordering wavevector, γ and ν are the usual susceptibility and correlation function exponents. That is $\chi \propto t^{-\gamma}$ and $\xi \propto t^{-\nu}$. We expect the usual scaling relationship $\gamma = (2 - \eta)\nu$.

If we are at the QCP, we have $t = 0$, since b is arbitrary, we can choose $b^z T = 1$, $b = T^{-1/z}$.

$$\chi(q, \omega, T) = b^{\gamma/\nu} \chi(bq, b^z \omega, b^z T), \quad (\text{S2})$$

$$= T^{-\frac{\gamma}{\nu z}} \chi(T^{-\frac{1}{z}} q, \frac{\omega}{T}, 1), \quad (\text{S3})$$

$$= T^{-\alpha} \Phi \left(\xi_T q, \frac{\hbar \omega}{k_B T} \right), \quad (\text{S4})$$

where $\alpha = \gamma/\nu z$, Φ is a complex function and $\xi_T \propto T^{-1/z}$ a thermal length.

Dynamic scaling at the ordering wavevector and QCP.

At the ordering wavevector ($q = 0$) we have

$$\chi''(q = 0, \omega, T) = T^{-\frac{\gamma}{\nu z}} \phi_1 \left(\frac{\hbar \omega}{k_B T} \right), \quad (\text{S5})$$

where $\phi_{\mathbb{P}}(x) = \Im[\Phi(0, x)]$ is a scaling function. Equation Eqn. S5 is known as ω/T -scaling.

ω/T scaling of $\kappa(\omega)$.

From Eqns. S4 and S5 we can write

$$\frac{\chi''(q, \omega)}{\chi''(q = 0, \omega)} = \phi_3 \left(\xi q, \frac{\hbar \omega}{k_B T} \right). \quad (\text{S6})$$

We can associate the second factor in Eqn. S10 with ϕ_3 in Eqn. S6. In order to interpret $\kappa(\omega)$ as a peak width, we set the factor to be a fraction β of the peak susceptibility at $q = \kappa(\omega)$ i.e.

$$\beta = \frac{\chi''(q, \omega)}{\chi''(q = 0, \omega)} \quad (\text{S7})$$

$$= \phi_3 \left(\xi \kappa, \frac{\hbar \omega}{k_B T} \right). \quad (\text{S8})$$

The implicit Eqn. S8 implies that there is a function $\phi_3(x)$ such that $\xi \kappa = \phi_2(\hbar \omega / k_B T)$ and therefore

$$\kappa(\omega) \propto T^{\frac{1}{z}} \phi_2 \left(\frac{\hbar \omega}{k_B T} \right) \quad (\text{S9})$$

Thus $\kappa(\omega)$ also shows ω/T scaling.

Phenomenological Model

We parameterize our normal-state data with a phenomenological susceptibility used by Aeppli *et al.* [1]:

$$\chi''(\mathbf{Q}, \omega) = \chi''(\mathbf{Q}_\delta, \omega) \frac{1}{[1 + \kappa^{-2}(\omega) R(\mathbf{Q})]^2}, \quad (\text{S10})$$

where

$$R(\mathbf{Q}) = \frac{1}{4\delta^2} \left\{ [(H - \frac{1}{2})^2 + (K - \frac{1}{2})^2 - \delta^2]^2 + 4(H - \frac{1}{2})^2 (K - \frac{1}{2})^2 \right\}. \quad (\text{S11})$$

$R(\mathbf{Q})$ has zeros at the positions $\mathbf{Q}_\delta = (1/2 \pm \delta, 1/2)$ and $(1/2 \pm \delta, 1/2)$ and this function approximately reproduces the \mathbf{Q} dependence of our data. Near each \mathbf{Q}_δ , $R(\mathbf{Q}_\delta + \mathbf{q}) = |\mathbf{q}|^2$.

We find experimentally that the susceptibility at \mathbf{Q}_δ has the form:

$$\chi''(\mathbf{Q}_\delta, \omega) = \frac{\chi'(\mathbf{Q}_\delta) \Gamma_\delta \omega}{\Gamma_\delta^2 + \omega^2} \quad (\text{S12})$$

The real part of the susceptibility $\chi'(\mathbf{Q}_\delta) \propto T^{-\alpha}$ and the spin relaxation rate varies as $\hbar \Gamma_\delta = a k_B T$. We also posit the form

$$\kappa^2(\omega) = \eta k_B^{-2/z} \left[(\hbar \omega)^{2/z} + (k_B T)^{2/z} \right]. \quad (\text{S13})$$

This has the ω/T scaling form (cf. Eqn. S9)

$$\kappa(\omega) = \eta T^{1/z} \left[1 + \left(\frac{\hbar\omega}{k_B T} \right)^{2/z} \right]. \quad (\text{S14})$$

Finally, combining Eqn. S12 & S13 and setting $R(\mathbf{Q}) = q^2$ we obtain:

$$\chi''(\mathbf{Q}, \omega) \propto \frac{T^{-\alpha} \left(\frac{\hbar\omega}{k_B T} \right)}{a^2 + \left(\frac{\hbar\omega}{k_B T} \right)^2} \times \frac{1}{\left(1 + \left[1 + \left(\frac{\hbar\omega}{k_B T} \right)^{2/z} \right]^{-2} \left(\frac{q}{\eta T^{1/z}} \right)^2 \right)^2}. \quad (\text{S15})$$

Eqn. S15 shows the scaling behaviour described by Eqn. S4.

$\kappa(\omega)$ fitting

In order to fit our data we use a generalized form of Eqn. S13:

$$\kappa^2(\omega) = \Delta + a_0^{-2} \left[\left(\frac{\hbar\omega}{E_\kappa} \right)^{2/z} + r \left(\frac{k_B T}{E_\kappa} \right)^{2/z} \right]. \quad (\text{S16})$$

We fit $\kappa(\omega, T)$ in units of \AA^{-1} to the model in Eqn. S16 fixing r to be 1 as has been found to be approximately true in LSCO $x=0.14$ [1]. Here Δ is a tuning parameter which is zero for a QCP, E_κ is an energy scale and a_0 is the in-plane lattice parameter. This fit gives $z = 1.83 \pm 0.35$, $\Delta = (4 \pm 14) \times 10^{-4} \text{\AA}^{-2}$ and $E_\kappa = 68 \pm 17$ meV. Thus Δ is zero within the resolution of the experiment. For the fitted values of z and a , the static correlations decay approximately with width $\kappa(0)^{-1}$.

Quantum phase transitions in metals with Harris disorder

This section recalls the theoretical model presented in Ref. [2], and describes the computation of its real frequency response functions. There is some overlap of the initial discussion here with the review in Ref. [3].

We focus on quantum fluctuations of the spin density wave (SDW) order parameter across the quantum phase transition from the Fermi liquid [4, 5]. We write the SDW order as ($a = x, y, z$)

$$S_a(\mathbf{r}) = \sum_{\ell} \phi_{\ell a} e^{i\mathbf{Q}_{\delta\ell} \cdot \mathbf{r}} \quad (\text{S17})$$

where S_a is the electron spin at position \mathbf{r} , $\ell = 1 \dots 4$ labels the 4 ordering wavevectors $\mathbf{Q}_{\delta\ell}$ at $(1/2, 1/2 \pm \delta)$

and $(1/2 \pm \delta, 1/2)$. We are interested in fluctuations of the SDW order parameters $\phi_{\ell a}$ coupled to electrons $c_{\mathbf{k}\sigma}$ with dispersion $\varepsilon(\mathbf{k})$ which has a Fermi surface. Including the effects of spatial disorder, we have a two-dimensional Yukawa-Sachdev-Ye-Kitev model with the imaginary time (τ) Lagrangian [6, 7]

$$\begin{aligned} \mathcal{L}_{YSYK} = & \sum_{\mathbf{k}} c_{\mathbf{k}\sigma}^\dagger \left(\frac{\partial}{\partial \tau} + \varepsilon(\mathbf{k}) \right) c_{\mathbf{k}\sigma} + \int d^2\mathbf{r} \left\{ \lambda [\phi(\mathbf{r})]^2 \right. \\ & + [g + g'(\mathbf{r})] \sum_{\ell} c_{\sigma}^\dagger(\mathbf{r}) \tau_{\sigma\sigma'}^a c_{\sigma'}(\mathbf{r}) \phi_{\ell a}(\mathbf{r}) e^{i\mathbf{Q}_{\delta\ell} \cdot \mathbf{r}} \\ & \left. + K [\nabla_{\mathbf{r}} \phi(\mathbf{r})]^2 + u [\phi(\mathbf{r})]^4 + v(\mathbf{r}) c_{\sigma}^\dagger(\mathbf{r}) c_{\sigma}(\mathbf{r}) \right\}. \end{aligned} \quad (\text{S18})$$

Here τ^a are the Pauli matrices, λ is the parameter employed to tune across the transition, and g is the Yukawa coupling between the fermions and bosons. We have included two sources of spatial randomness. The spatially random potential $v(\mathbf{r})$, with ensemble averages $\overline{v(\mathbf{r})} = 0$, $\overline{v(\mathbf{r})v(\mathbf{r}')} = v^2 \delta(\mathbf{r} - \mathbf{r}')$, acts on the fermion density, and plays a central role in the theory of disorder-induced electron localization [8]. Such fermion localization effects are also present here, but all indications are that such effects are not important for the cuprates. Instead, our focus will be on the more relevant ‘Harris disorder’, induced by spatial randomness in the position of the quantum critical point. Following Ref. [7], we have represented this by a spatially random Yukawa coupling $g'(\mathbf{r})$ with $\overline{g'(\mathbf{r})} = 0$, $\overline{g'(\mathbf{r})g'(\mathbf{r}')} = g'^2 \delta(\mathbf{r} - \mathbf{r}')$. A more conventional form of Harris disorder is a random tuning parameter $\lambda \rightarrow \lambda + \delta\lambda(\mathbf{r})$, but this can be transferred to $g'(\mathbf{r})$ by a \mathbf{r} -dependent rescaling of ϕ . In both forms, Harris disorder leads to boson localization at low temperatures [2, 9], where it must be treated non-perturbatively, as we do below. But in higher temperature regimes, where the bosons do not localize, we can add a large number of flavor labels to the fields so that the $g'(\mathbf{r})$ disorder in (S18) is amenable to self-consistent disorder averaged solution which is exact in a large flavor solution [6, 7, 10].

Patel *et al.* [9] have studied the YSYK model (S18) at $g = 0$ by large scale, high precision quantum Monte Carlo simulations (with no additional flavors), and their results for the imaginary time spin susceptibility appear in Fig. 4E of the main text. We describe below the approach used in Ref. [2] which treats the interactions in a mean-field manner, but accounts for disorder numerically exactly; this approach has the advantage of allowing exact analytic continuation to real frequencies at arbitrary temperatures. The results of Ref. [2] are in general agreement with the exact Monte Carlo results of Ref. [9]: both show an extended quantum Griffiths phase with ω/T scaling, but the value of α is smaller and more reliable in the Monte Carlo study.

The approach of Ref. [2] is to integrate out the fermions from (S18) (assuming fermionic eigenmodes remain extended), and consider the resulting Landau-

damped Hertz-Millis theory for the boson ϕ alone. The spatial disorder in the Yukawa coupling $g'(\mathbf{r})$ will lead to disorder in all couplings in the effective boson theory. For simplicity, we retain only the most relevant 'random mass' disorder in the tuning parameter $\lambda \rightarrow \lambda + \delta\lambda(\mathbf{r})$. We also drop the longer-range RKKY couplings between the ϕ that will be induced by integrating out the fermions [11]. We discretize the boson theory on a lattice of sites (labeled by j), and write the SDW order parameters in terms of a real ϕ with a single index $a = 1 \dots M$ with $M = 12$. In this manner, we obtain the action

$$\begin{aligned} \mathcal{S} &= \mathcal{S}_\phi + \mathcal{S}_{\phi d} \\ \mathcal{S}_\phi &= \int d\tau \left[\frac{J}{2} \sum_{\langle ij \rangle} (\phi_{ia} - \phi_{ja})^2 + \sum_j \left\{ \frac{\lambda + \delta\lambda_j}{2} \phi_{ja}^2 + \frac{u}{4M} (\phi_{ja}^2)^2 \right\} \right] \\ \mathcal{S}_{\phi d} &= \frac{T}{2} \sum_{\Omega} \sum_j (\gamma|\Omega| + \Omega^2/c^2) |\phi_{ja}(i\Omega)|^2, \end{aligned} \quad (\text{S19})$$

where Ω is a Matsubara frequency at a temperature T , γ is the Landau damping, and the Ω^2/c^2 term has been inserted as a high frequency cutoff. The random mass disorder satisfies $\delta\lambda(\mathbf{r}) = 0$, $\delta\lambda(\mathbf{r})\delta\lambda(\mathbf{r}') = \delta\lambda^2\delta(\mathbf{r} - \mathbf{r}')$. For simplicity, we have assumed a global $O(M)$ symmetry, but this assumption can be relaxed without significantly modifying the results.

The theory in (S19) has been studied using a strong disorder renormalization group [12–14]. But the same basic results are obtained by the method of Ref. [2] (originally used for a related problem in $d = 1$ in Ref. [15]), which also allows study of the crossover at higher energies to weak disorder, and this will be important for our purposes. Following Refs. [2, 15], we replace \mathcal{S}_ϕ by an effective quadratic action, while renormalizing the space dependent mass in a self-consistent manner; this leads to

$$\begin{aligned} \tilde{\mathcal{S}}_\phi &= \int d\tau \left[\frac{J}{2} \sum_{\langle ij \rangle} (\phi_{ia} - \phi_{ja})^2 + \sum_j \frac{\tilde{\lambda}_j}{2} \phi_{ja}^2 \right] \\ \tilde{\lambda}_j &= \lambda + \delta\lambda_j + \frac{u}{M} \sum_a \langle \phi_{ja}^2 \rangle_{\tilde{\mathcal{S}}_\phi + \mathcal{S}_{\phi d}} \\ &= \lambda + \delta\lambda_j + uT \sum_{\Omega} \sum_b \frac{\psi_{bi}\psi_{bj}}{\gamma|\Omega| + \Omega^2/c^2 + e_b}, \end{aligned} \quad (\text{S20})$$

where e_b and ψ_{bj} are eigenvalues and eigenfunctions of the ϕ quadratic form in $\tilde{\mathcal{S}}_\phi$, labeled by the index $b = 1 \dots L^2$ for a $L \times L$ sample. For each disorder realization δs_j , the values of $\tilde{\lambda}_j$ are determined by numerically solving (S20), and this also yields results for the eigenvalues e_b and the eigenvectors ψ_{bj} . The dynamic spin susceptibility is then computed at a real frequency

ω from

$$\chi_{ij}(\omega) = \sum_b \frac{\psi_{bi}\psi_{bj}}{-i\gamma\omega - \omega^2/c^2 + e_b}, \quad (\text{S21})$$

followed by a Fourier transform from spatial co-ordinates to momenta.

Results from the computation above are presented in Fig. 4 of the main text, and Figs. 1-9 below. The chosen parameter values are $J = 1$, $\gamma = 1$, $c^2 = 10$, $u = 1$ and $\delta\lambda^2 = 0.25$. The quantum critical point at $T = 0$ is at $\lambda_c = -0.4586$ and the quantum Griffiths phase begins at $\lambda_G = -0.4300$ [2]. We used a system size of 160×160 and averaged over 20 disorder realizations. We can set the energy scale by identifying the highest energy spin excitation ($c\sqrt{8J} \approx 9$ with the highest energy spin wave (≈ 300 meV [16]). This leads to the estimate $300/9 \approx 33$ meV as the unit of energy for the numerics.

The results for the dynamic spin susceptibility at the ordering wavevector \mathbf{Q}_δ were shown in Fig. 4 of the main text for $\lambda = \lambda_c$, where we found good ω/T scaling. Fig. 1 extends these results to $\lambda > \lambda_c$. Now we find ω/T scaling only for smaller values of ω/T . This restriction of ω/T scaling to $\omega \lesssim T$ for $\lambda > \lambda_c$ is not at odds with the experimental results in the main text, which also, strictly speaking, establish ω/T scaling for $\omega \lesssim T$ as the range of ω values available is not enough to achieve larger values of ω/T at the larger values of T that are considered.

The value of the exponent α decreases monotonically with increasing distance from the critical point (increasing λ). In Fig. 2, we show that using a smaller value of α makes little difference to the quality of the fit at small ω/T , which is the region at which scaling is established in the observations.

Similar features are present in the quantum Monte Carlo results [9] discussed in Fig. 4 of the main text, where λ_s is analogous to λ_c . For $\lambda > \lambda_s$ and approaching the beginning of the Griffiths phase at $\lambda = \lambda_G$, only the zeroth Matsubara frequency scales as $\chi(\omega = 0) \sim T^{-\alpha}$ (with a value of α that is smaller than that at $\lambda = \lambda_s$) while the nonzero ones do not, implying that ω/T scaling is restricted to frequencies $\omega < 2\pi T$.

Fig. 3 shows similar results for the *local* dynamic spin susceptibility

$$\chi_L''(\omega) = \int \frac{d^2\mathbf{q}}{4\pi^2} \chi''(\mathbf{q}, \omega) \quad (\text{S22})$$

for $\lambda \geq \lambda_c$.

Now we find that ω/T scaling holds for all values λ , an indication that the criticality for $\lambda > \lambda_c$ is from localized spin fluctuations. This is just as expected from a quantum Griffiths critical phase. By scaling, the exponent for the local susceptibility $\alpha + \mu = 2/z$, and this is consistent with our values $\mu = 0.1$ to 0.16 , $\alpha = 0.84$ to 0.59 and $z = 2.1$ to 2.6 respectively for the range of $\lambda = -0.4586$ to -0.4300 considered.

Fig. 4 extends the analysis of scaling for the local and ordering wavevector susceptibilities at $\lambda = \lambda_c$ to much lower values of T , showing a breakdown of ω/T scaling at low T .

This is consistent with results for the boson density of states in Ref. [9], which showed a crossover from the constant density of states associated with marginal Fermi liquid behavior at higher energy, to a regime dominated by Griffiths effects at lower energy. The breakdown of ω/T scaling here in the dynamic spin susceptibility likely arises from the enhanced boson density of states at smallest energies, and could possibly be captured by experiments at lower temperatures than the ones considered in this work.

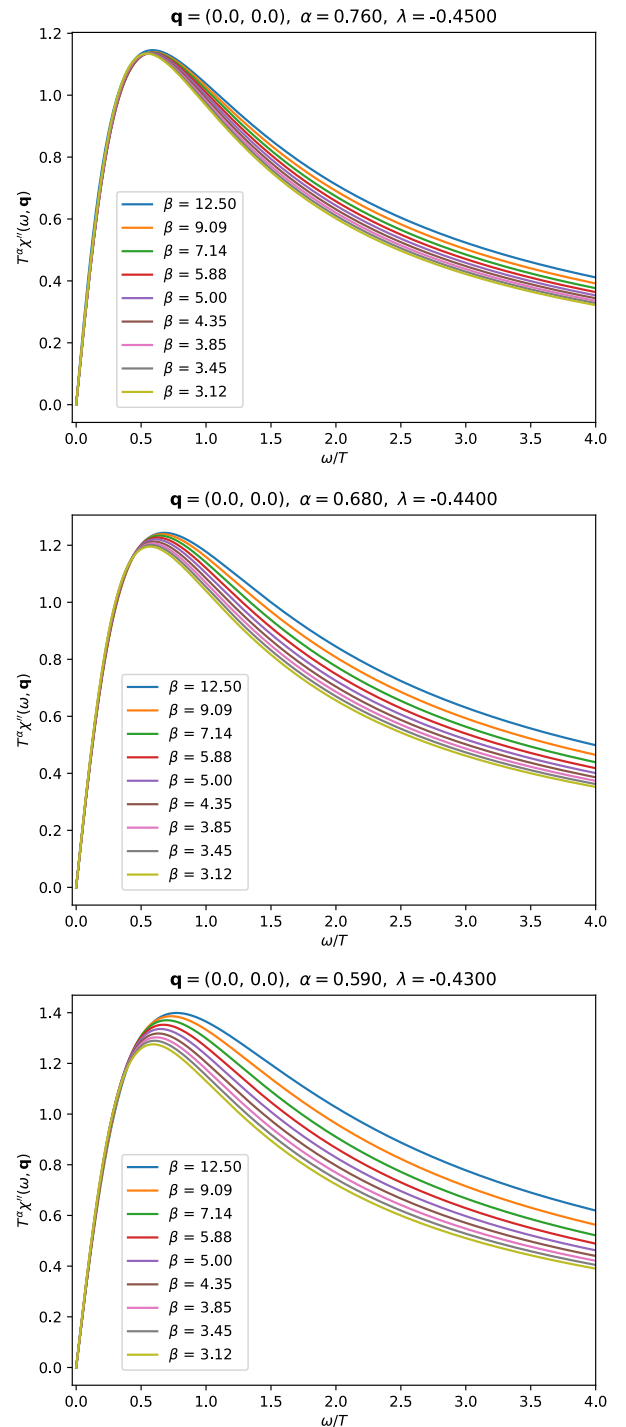
Next, we turn to the behavior of the inverse correlation length, κ , defined by (6) in the main text (also (S10)). Given the parameterization in (S17), the dynamic susceptibility is represented by a sum of contributions in the vicinity of the $\mathbf{Q}_{\delta\ell}$, each of which is discretized on the square lattice. Consequently, it is appropriate to adapt (S10) to

$$\frac{\chi''(\mathbf{q}, \omega)}{\chi''(\mathbf{q} = 0, \omega)} = \frac{\kappa^4(\omega)}{[\kappa^2(\omega) + 4 - 2\cos(q_x) - 2\cos(q_y)]^2}. \quad (\text{S23})$$

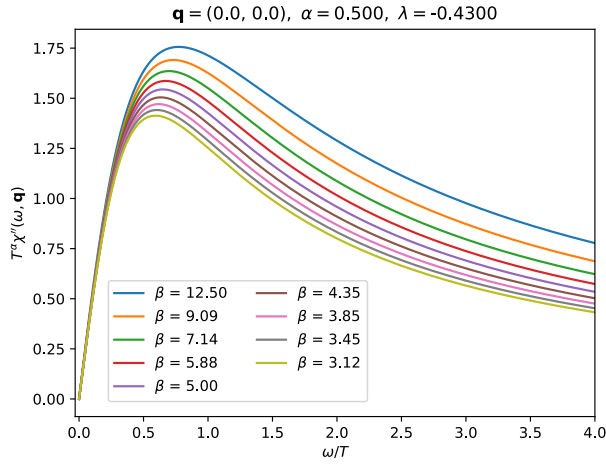
Fig. 5 shows that (S23) provides an excellent fit to the numerical data, and this enables determination of $\kappa(\omega, T)$. Our results for κ and their scaling are shown in Fig. 4C,D of the main text at $\lambda = \lambda_c$. Corresponding results for $\lambda > \lambda_c$ appear in Figs. 6 and 7.

As for the dynamics spin susceptibility at the ordering wavevector, ω/T scaling works for $\lambda = \lambda_c$, but only for smaller values of ω/T for $\lambda > \lambda_c$. The plots of Fig. 7 are shown on a logarithmic frequency scale in Fig. 8 (as in Figs. 3 and 4D of the main text), which exposes the lower frequency range.

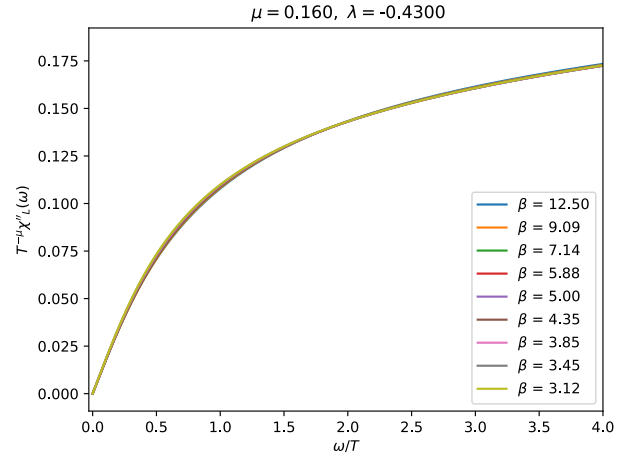
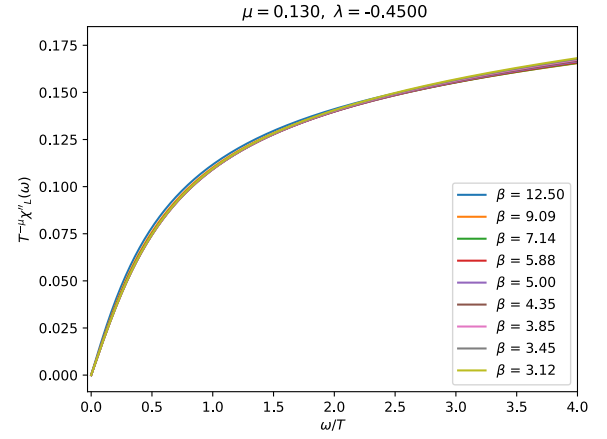
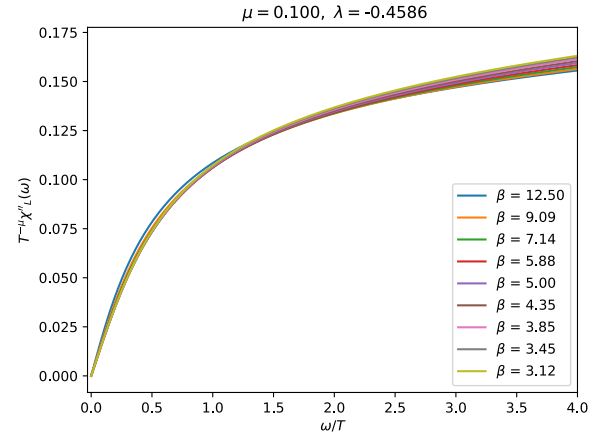
Finally, we complement plots of the resistivity induced by the disordered spin fluctuations in Fig. 4 of the main text at additional values of λ in Fig. 9. The resistivity was computed from the numerical results for $\chi''_L(\omega)$, as specified in Ref. [2].



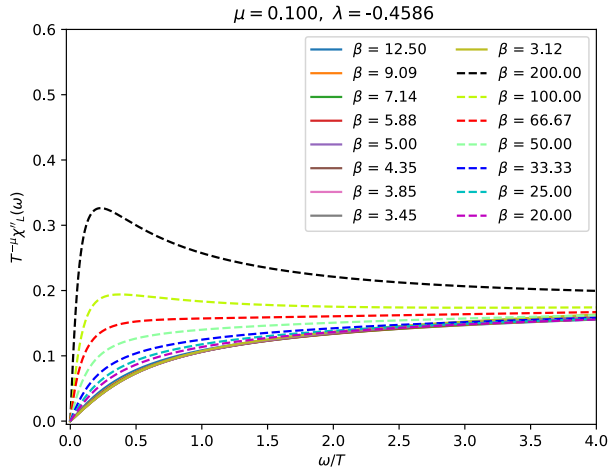
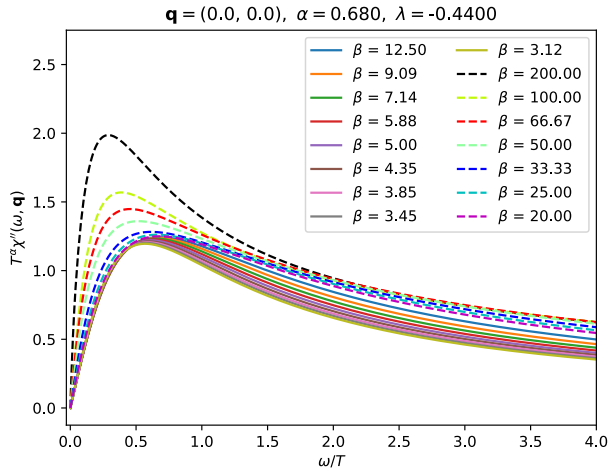
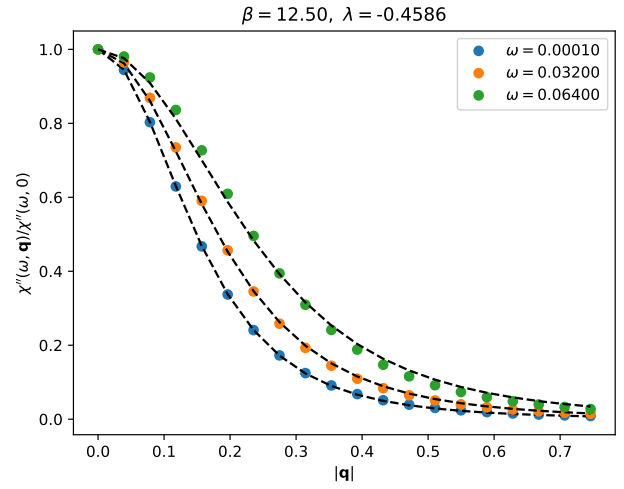
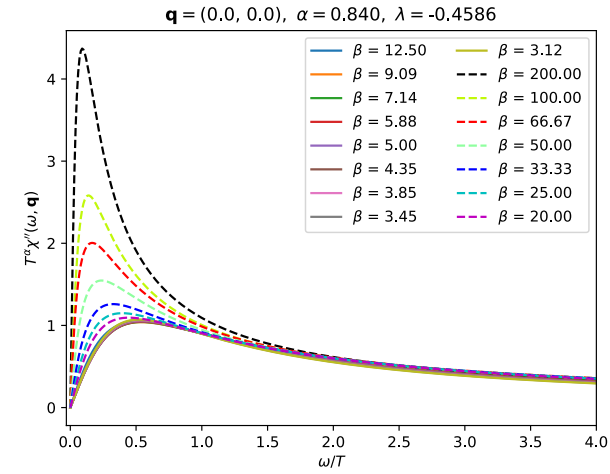
Supplementary Fig. 1. **Scaling plots of the dynamic spin susceptibility at the ordering wavevector for $\lambda > \lambda_c = -0.4586$.** Results for $\lambda = \lambda_c$ are in Fig. 4B in the main text.



Supplementary Fig. 2. **Scaling plots of the dynamic spin susceptibility at the ordering wavevector for $\lambda = -0.43$.** A smaller value of the exponent α is used in comparison to the corresponding plot in Fig. 1.

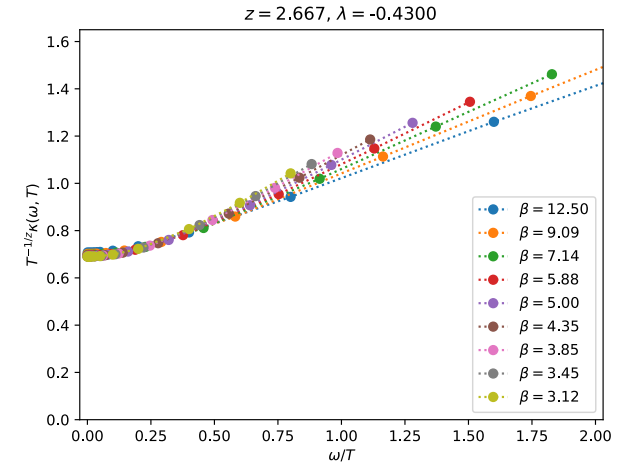
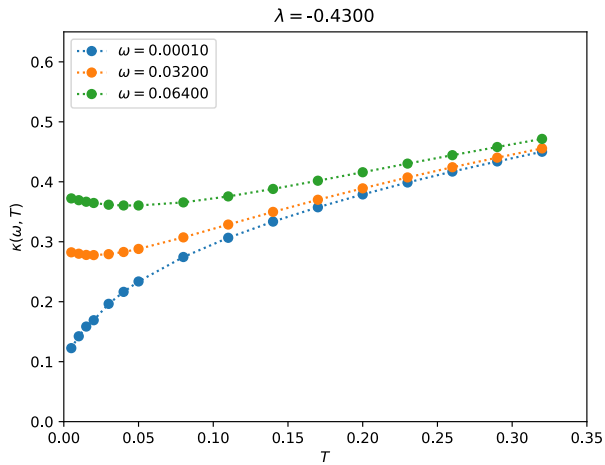
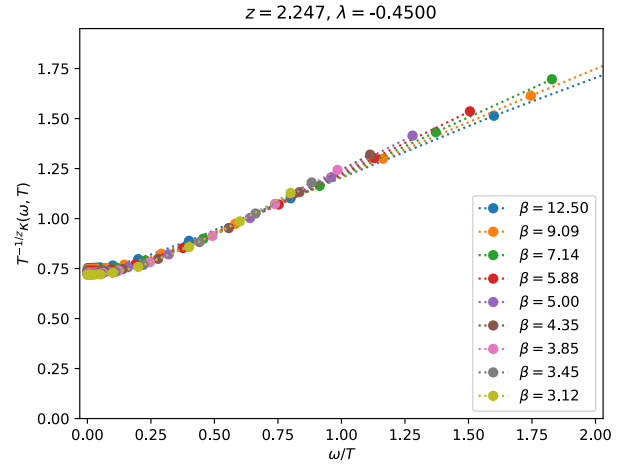
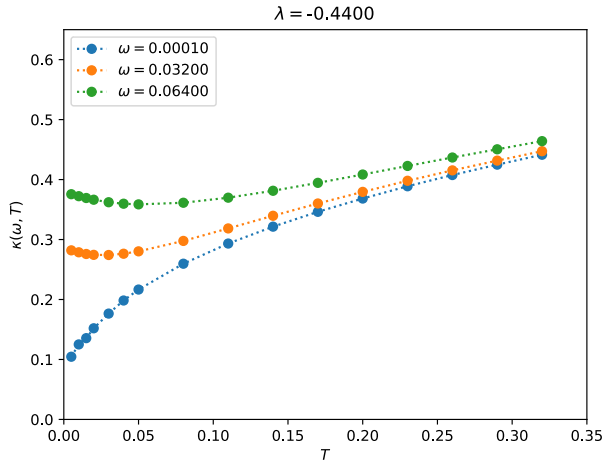
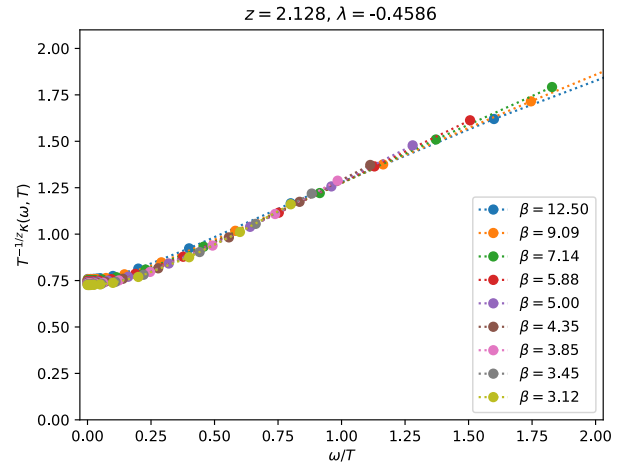
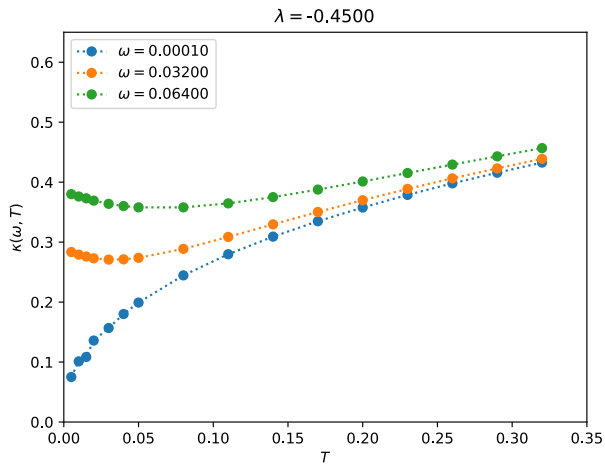


Supplementary Fig. 3. **Scaling plots of the local dynamic spin susceptibility for $\lambda \geq \lambda_c = -0.4586$.**



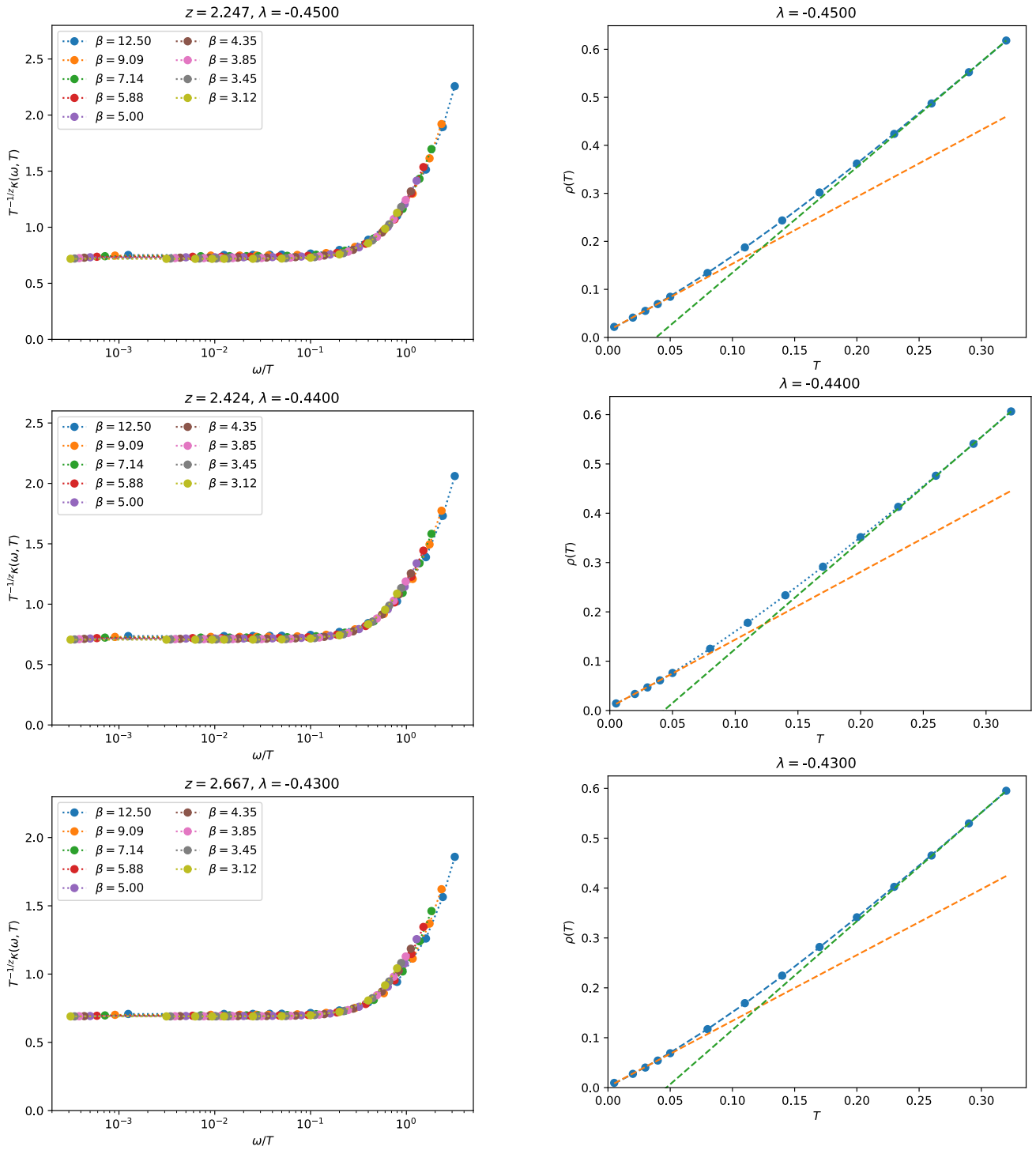
Supplementary Fig. 5. Fits of the dynamic spin susceptibility to (S23), allowing determination of $\kappa(\omega, T)$.

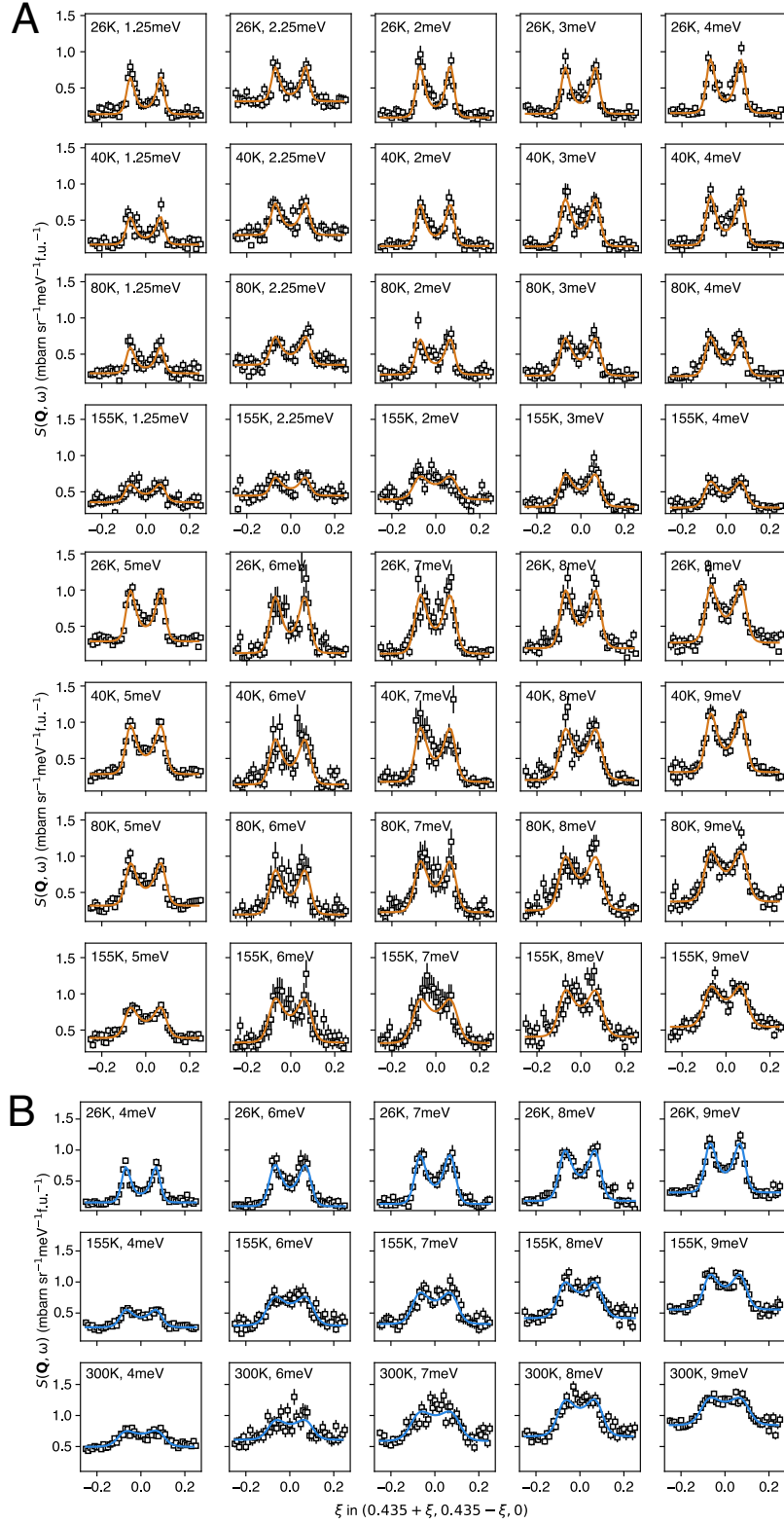
Supplementary Fig. 4. **Breakdown of scaling at very low temperatures.** The dynamic susceptibilities at lower temperatures. Compare to the plots in Fig. 4 of the main text and Fig. 3.



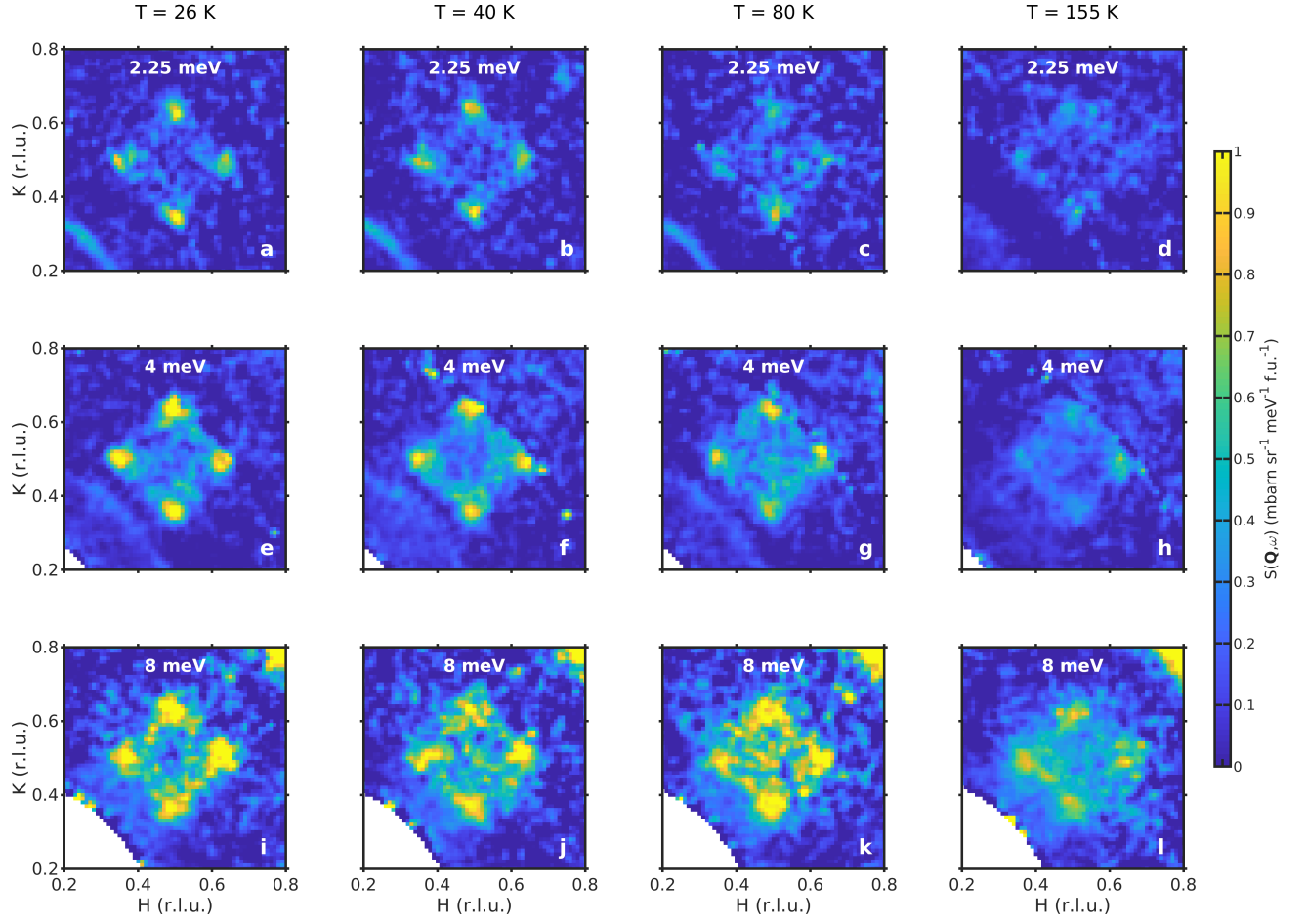
Supplementary Fig. 6. **Plots of κ for $\lambda > \lambda_c = -0.4586$.** Results for $\lambda = \lambda_c$ are in Fig. 4C in the main text.

Supplementary Fig. 7. **Scaling plots of κ for $\lambda \geq \lambda_c = -0.4586$.**

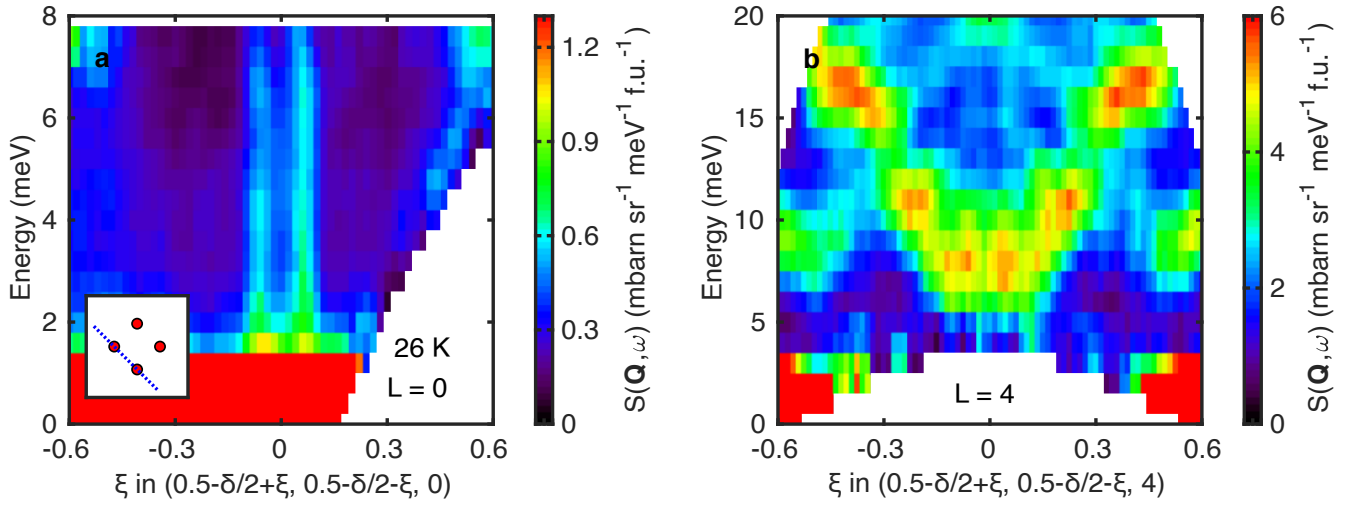




Supplementary Fig. 10. A representative selection of $S(\mathbf{Q}, \omega)$ cuts and fits to the model described in the main text. (A) Experiment 1. (B) Experiment 2.



Supplementary Fig. 11. Slices of $S(\mathbf{Q}, \omega)$ with subtraction of a flat background (see section 2-D \mathbf{Q} Slices) for various energies and temperatures. Data at $T=26$ K, 40 K and 80 K is from experiment 1 and $T=155$ K from experiment 2.



Supplementary Fig. 12. **Spin fluctuations and phonons in $\text{La}_{2-x}\text{Sr}_x\text{CuO}_4$ ($x = 0.22$) near \mathbf{Q}_δ .** $S(\mathbf{Q}, \omega)$ as a function of energy and wavevector along a trajectory through two incommensurate wave vectors $\mathbf{Q}_\delta = (0.5-\delta, 0.5, L)$ and $(0.5, 0.5-\delta, L)$ (see inset to panel **a**). Integration ranges are **a** $L \in [-1, 1]$ and **b** $L \in [3.8, 4.2]$. Strong phonons are observed (panel **b**) for $L \approx 4$, but these are not visible near $L = 0$ (panel **a**) where spin fluctuations are seen. Data were collected on LET (panel **a**) and MERLIN (panel **b**).

SUPPLEMENTARY REFERENCES

- [1] G. Aeppli, T. Mason, S. Hayden, H. Mook, and J. Kulda, *Science* **278**, 1432 (1997).
- [2] A. A. Patel, P. Lunts, and S. Sachdev, *Proc. Natl. Acad. Sci.* **121**, e2402052121 (2024).
- [3] S. Sachdev, *Physica C* **633**, 1354707 (2025).
- [4] J. A. Hertz, *Phys. Rev. B* **14**, 1165 (1976).
- [5] A. J. Millis, *Phys. Rev. B* **48**, 7183 (1993).
- [6] I. Esterlis, H. Guo, A. A. Patel, and S. Sachdev, *Phys. Rev. B* **103**, 235129 (2021).
- [7] A. A. Patel, H. Guo, I. Esterlis, and S. Sachdev, *Science* **381**, 790 (2023).
- [8] P. A. Lee and T. V. Ramakrishnan, *Rev. Mod. Phys.* **57**, 287 (1985).
- [9] A. A. Patel, P. Lunts, and M. S. Albergo, *Phys. Rev. X* **15**, 031064 (2025).
- [10] C. Li, D. Valentinis, A. A. Patel, H. Guo, J. Schmalian, S. Sachdev, and I. Esterlis, *Phys. Rev. Lett.* **133**, 186502 (2024).
- [11] J. H. Van Vleck, *Rev. Mod. Phys.* **34**, 681 (1962).
- [12] J. A. Hoyos, C. Kotabage, and T. Vojta, *Phys. Rev. Lett.* **99**, 230601 (2007).
- [13] T. Vojta, C. Kotabage, and J. A. Hoyos, *Phys. Rev. B* **79**, 024401 (2009).
- [14] T. Vojta, in *Lectures on the Physics of Strongly Correlated Systems XVII: Seventeenth Training Course in the Physics of Strongly Correlated Systems*, American Institute of Physics Conference Series, Vol. 1550, edited by A. Avella and F. Mancini (AIP, 2013) pp. 188–247, arXiv:1301.7746 [cond-mat.dis-nn].
- [15] A. Del Maestro, B. Rosenow, M. Müller, and S. Sachdev, *Phys. Rev. Lett.* **101**, 035701 (2008).
- [16] S. M. Hayden, G. Aeppli, R. Osborn, A. D. Taylor, T. G. Perring, S. W. Cheong, and Z. Fisk, *Phys. Rev. Lett.* **67**, 3622 (1991).